Institute of High Energy Physics
Chinese Academy of Sciences

ERROR AND CORRECTION SIMULATION OF CEPC BOOSTER AND DAMPING RING

Daheng Ji†, Dou Wang

IHEP, CAS, Beijing 100049, China

Error Set

Parameters	Dipole	Quadrupole	Sextupole
Transverse shift X/Y (μm)	100	100	100
Longitudinal shift Z (μm)	100	150	100
Tilt about X/Y (mrad)	0.2	0.2	0.2
Tilt about Z (mrad)	0.1	0.2	0.1
Nominal field	1×10^{-3}	2×10^{-4}	3×10^{-4}

Parameters	BPM (10 Hz)
Accuracy (m)	1×10^{-7}
Tilt (mrad)	10
Gain	5%
Offset after beam based alignment (BBA) (mm)	30×10^{-3}

Correction Process

Orbit Correction + Horizontal dispersion
- Response Matrix
- 2-level iteration：
  - 1st Loop: 20%~100% Corrector
  - 2nd Loop：30%~80% SVD
- Dispersion correction
- Energy adjustment by corrector

Optics correction
- RM + LOCO
- Based on 30GeV simulation
- All quadrupole independent
- Dispersion correction included

Dispersion correction included
- Coupling and vertical dispersion correction
- Skew quadrupole magnets are arranged in both the dispersion free section and the arc section.

Booster Design update

To reduce emittance, costs and sensitivity
- TME like structure (cell length=78m)
- Interleave sextupole scheme
- Overall idea: uniform distribution for the Q
- Combined magnet (B+S) scheme possible
- Phase advance/cell: 100° (H) / 28° (V)
- Emittance@120GeV=1.26nm

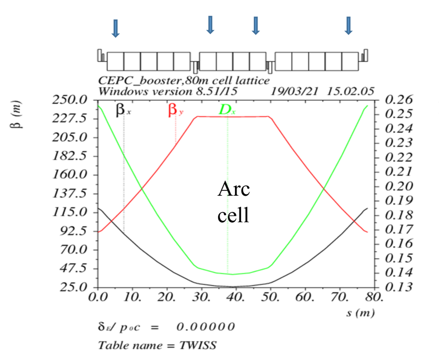
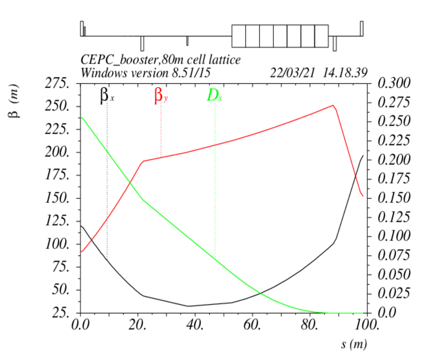
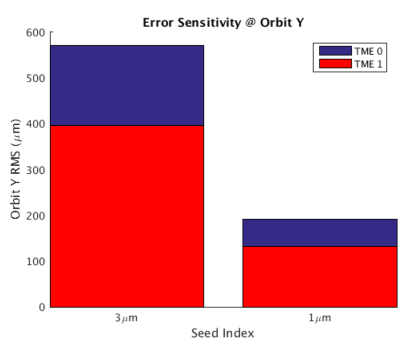

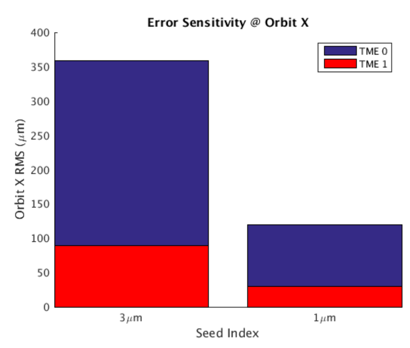

Booster Beam parameter with correction

RMS@30GeV	X	Y
Orbit (mm)	0.080	0.080
Beta Beating(%)	0.8	0.38
Δ Dispersion(mm)	2.7	3.5

Damping RING Design

Phase/cell: 60° /60°
Interleave sextupole scheme
2 sex. families

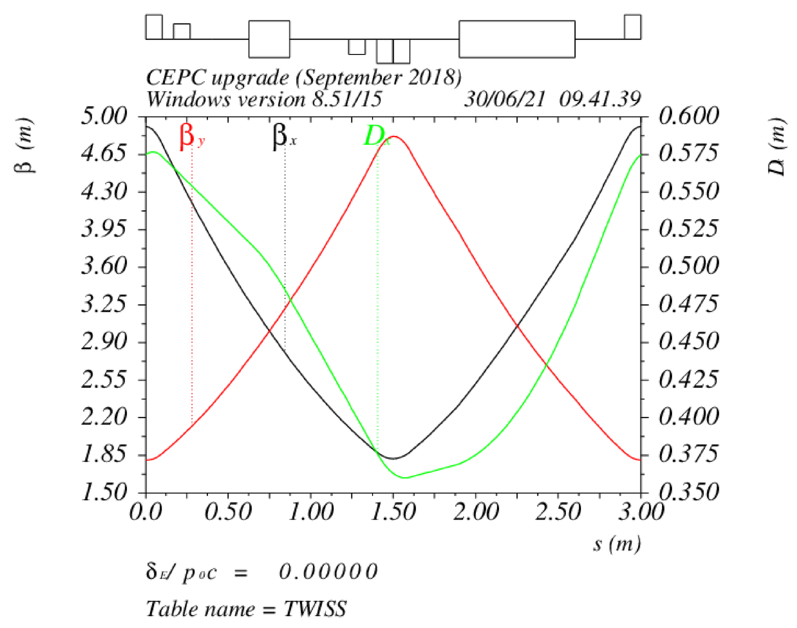

Damping Ring parameter with correction

RMS@30GeV	X	Y
Orbit (mm)	0.58	0.56
Beta Beating(%)	1.1	2.0
Δ Dispersion(mm)	6.4	2.4

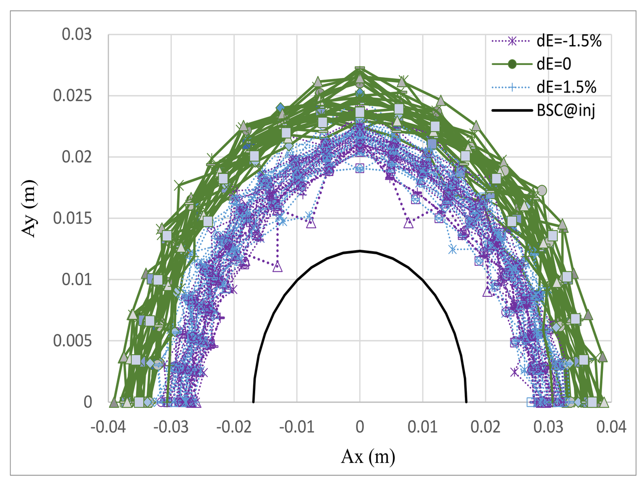

- $BSC_{x,y}=5\sigma_{inj_x,y}+5$mm
- Energy acceptance: $8.3\delta_{inj}=1.5\%$

DA@30GeV

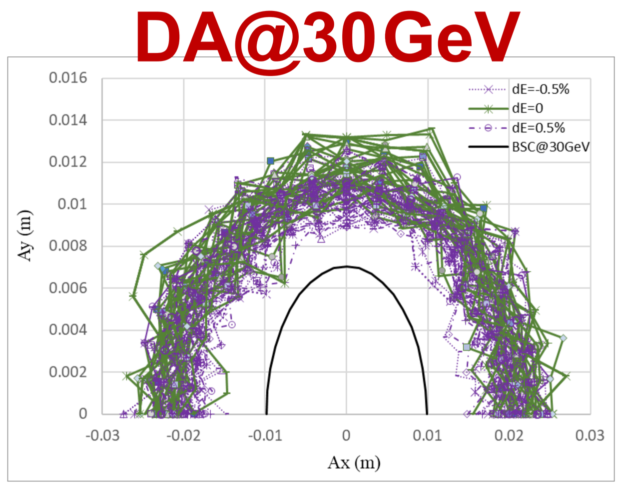

DA@45GeV

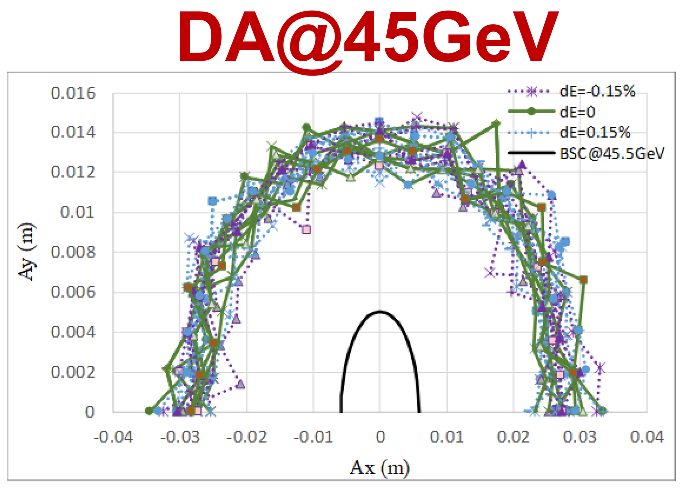

DA@80GeV

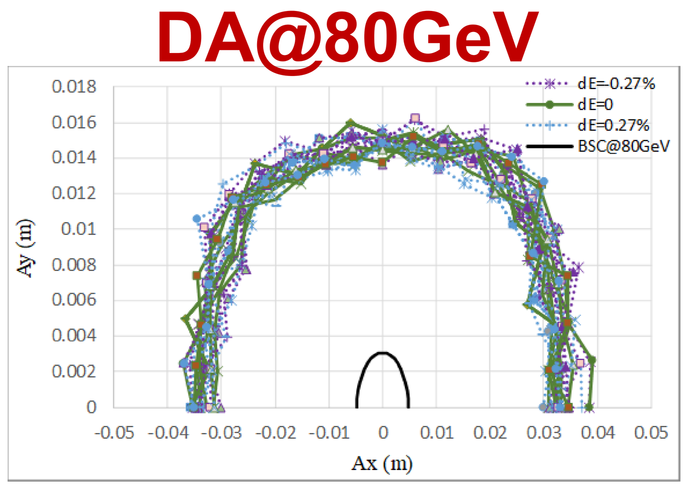

DA@120GeV

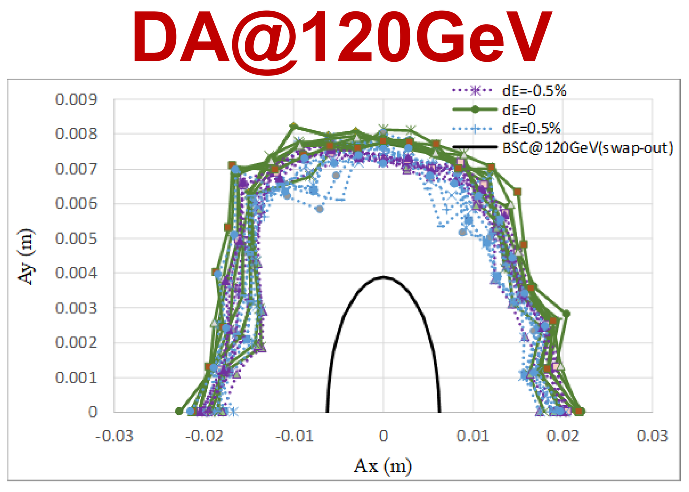

DA@180GeV

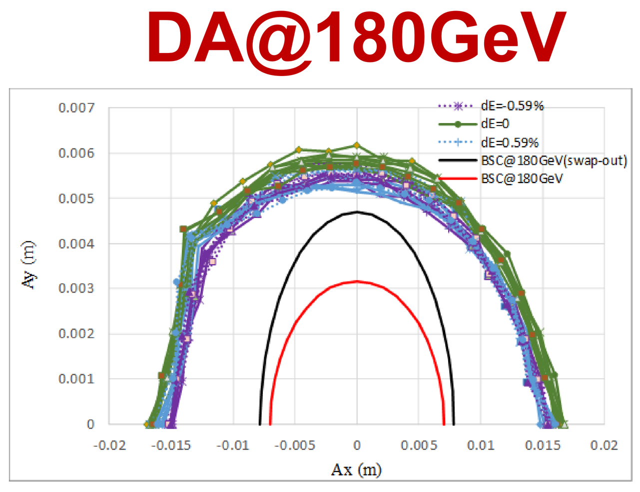

Summary

The TME structure (TDR) has combined magnets to reduce mounts, minimize beam emittance, optimize error sensitivity, simulate error effects and corrections, and determine hardware system requirements, with a clear simulation process showing that linear parameters and DA meet the requirements. Further studies will prioritize actual commissioning requirements..

† jidh@ihep.ac.cn

The Model and Particle-in-cell Simulation of Three-Dimensional Betatron Oscillation in Plasma Wakefield Acceleration

Yulong Liu*[1], Ming Zeng[1], Weiming An[2], Dazhang Li[1]

[1]Institute of High Energy Physics, Chinese Academy of Sciences, Beijing 100049, China and University of Chinese Academy of Sciences, Beijing 100049, China

[2]Department of Astronomy, Beijing Normal University, Beijing 100875, China

1. Introduction

Betatron oscillation is an important phenomenon of electrons in plasma wakefield acceleration. During the process of oscillation, electrons emit synchrotron radiation, which affects the electrons in return. The force reacted on the electrons itself is called the radiation reaction (RR). Theoretically, we have built an three-dimensional betatron oscillation model with RR to describe the long-distance wakefield acceleration. In the model, long-term equations (LTE) are obtained by averaging the motion of the electron in the betatron time scale. In simulation, however, the process has not be simulated yet by QuickPIC, in the particle pusher module of which the longitudinal velocity of an electron is set to the speed of light while the transverse velocity and the radiation reaction are ignored. To solve the problem, we used Boris algorithm to solve for the motion of electrons in the three-dimensional wake, and added radiation reaction to the equations of motion. Finally, two phenomena predicted by the model are observed in simulation results, i.e. the precession movement of the elliptical betatron trajectory in the betatron phase shift dominant regime, and the tapering effect of the elliptical betatron trajectory in the radiation reaction dominant regime.

2. The motion of single electron

Neglecting the interaction between beam particles, the expression of wakefield is:

$$E_z = E_{z0} + \lambda\zeta_1,$$
$$E_r = \kappa^2(1-\lambda)r,$$
$$B_\theta = -\kappa^2\lambda r,$$

Where $\zeta = z - \beta_w t$, E_{z0} is the electric field at $\zeta = \langle\zeta\rangle$, $\langle\zeta\rangle$ is the average of ζ and ζ_1 is the high-frequency term of ζ. λ is the slope of longitudinal electric field at $\zeta = \langle\zeta\rangle$ and κ^2 is the coefficient of restoring force (generally 1/2).

RR is the dominate force when $k_p r_e\langle\gamma\rangle^{5/2} \gg 1$:

$$F_\mu^{rad} \approx \frac{2}{3} r_e \left(\frac{dP_\nu}{d\tau}\frac{dP^\nu}{d\tau}\right) P_\mu, \quad \text{or } \vec{f}^{rad} = \frac{2}{3} r_e \gamma\left(\dot{\gamma}^2 - \dot{p}_x{}^2 - \dot{p}_y{}^2 - \dot{p}_z{}^2\right)\vec{p}.$$

3. The long-term equations

Area in transverse phase space:

$$\dot{S}_x = -\frac{1}{8}\left[\frac{1}{4}\lambda\beta_{z0} - \kappa^2(1-2\lambda)\right]\langle\gamma\rangle^{-2} S_x S_y \sin 2\Delta\Phi - \frac{1}{4} r_e \kappa^3 \langle\gamma\rangle^{1/2}\left(S_x^2 + \frac{4-\cos 2\Delta\Phi}{3} S_x S_y\right),$$

$$\dot{S}_y = \frac{1}{8}\left[\frac{1}{4}\lambda\beta_{z0} - \kappa^2(1-2\lambda)\right]\langle\gamma\rangle^{-2} S_x S_y \sin 2\Delta\Phi - \frac{1}{4} r_e \kappa^3 \langle\gamma\rangle^{1/2}\left(S_y^2 + \frac{4-\cos 2\Delta\Phi}{3} S_x S_y\right),$$

Transverse phase difference:

$$d\Delta\Phi/dt = \frac{1}{8}\left[\frac{1}{4}\lambda\beta_{z0} - \kappa^2(1-2\lambda)\right]\langle\gamma\rangle^{-2}(S_y - S_x)\sin^2\Delta\Phi - \frac{1}{24} r_e \kappa^3 \langle\gamma\rangle^{1/2}(S_x + S_y)\sin 2\Delta\Phi,$$

Longitudinal shift:

$$\langle\dot{\zeta}\rangle = \frac{1}{2}\gamma_w^{-2} - \frac{1}{2}\langle\gamma\rangle^{-2} - \frac{1}{4}\kappa\langle\gamma\rangle^{-3/2}(S_x + S_y),$$

Average energy:

$$\langle\dot{\gamma}\rangle = -E_{z0}(\langle\zeta\rangle)\beta_{z0} - \frac{1}{3} r_e \kappa^3 \langle\gamma\rangle^{3/2}(S_x + S_y).$$

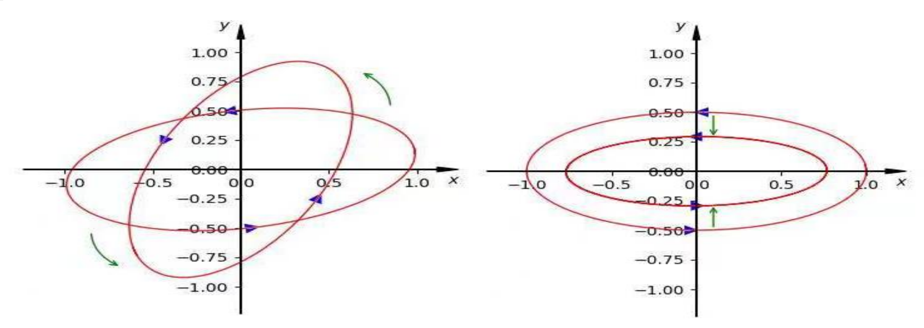

(a) (b)

Figure 1. Evolution of the particle trajectory (red ellipse) in the x-y plane. The blue arrows indicate the rotating direction of the particle. (a) In the betatron phase shift dominant regime, (b) In the radiation reaction dominant regime.

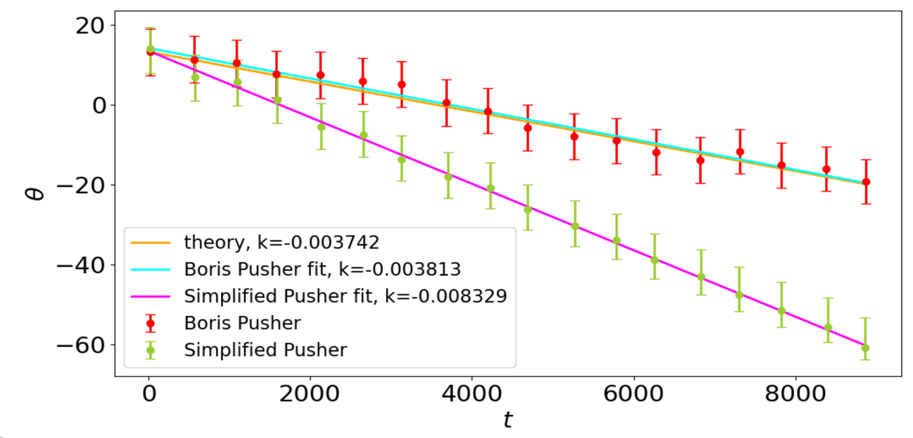

Figure 2. The angle θ of the major axis of the elliptical betatron trajectory changing with time. The difference of results between Boris Pusher and theory model is 1.90% while between Simplified Pusher and theory model is 123%.

[1] W. An, https://gitee.com/bnu-plasma-astrophysics-sg/quick-pic-open-source.git.
[2] M. Zeng , https://github.com/mingzeng7/PTrakcer , particle tracing code.
[3] Yulong Liu and Ming Zeng, Phys. Rev. Accel. Beams 26, 031301 (2023).
[4] I. Y. Kostyukov et al., Phys. Rev. ST Accel. Beams 15, 111001 (2012).
[5] C. Huang et al. Journal of Computational Physics 217 (2006).
[6] W. An et al, J. Comput. Phys. 250 (2013) 165-177.
[7] Viktor K. Decyk et al, CPC 282 (2023).

4. Betatron phase shift dominant regime ($k_p r_e\langle\gamma\rangle^{5/2} \ll 1$)

Angular velocity of the precession movement of the elliptical betatron trajectory :

$$\frac{d\theta}{dt} = -\frac{1}{8}\left[\frac{1}{4}\lambda v_{z0} - \kappa^2(1-2\lambda)\right]\langle\gamma\rangle^{-2} L_z,$$

where θ is the angle of the major axis of the ellipse (from particle trajectory in the betatron time scale) and L_z is the longitudinal angular momentum of the electron.

Transverse phase space area is conserved: $\frac{d(S_x+S_y)}{dt} = 0.$

5. Radiation reaction dominant regime ($k_p r_e\langle\gamma\rangle^{5/2} \gg 1$)

Area in transverse phase space decreases and the difference between Simplified_RR Pusher and Boris_RR Pusher can be ignored:

$$\frac{d(S_x+S_y)}{dt} = -\frac{1}{4} r_e \kappa^3 \langle\gamma\rangle^{\frac{1}{2}}\left[S_x^2 + S_y^2 + \frac{2(4-\cos 2\Delta\Phi)}{3} S_x S_y\right].$$

6. Five types of particle pushers

Frozen Pusher： keeping uniform motion in the longitudinal direction and stationary motion in the transverse direction;

Simplified Pusher（$v_z = c$）： $f_x = -E_x + B_y$， $f_y = -E_y - B_x$， $f_z = -E_z$;

Simplified_RR Pusher： considering RR based on Simplified Pusher;

Boris Pusher： using Boris algorithm， $\vec{f} = -\vec{E} - \vec{v} \times \vec{B}$;

Boris_RR Pusher： considering RR based on Boris Pusher.

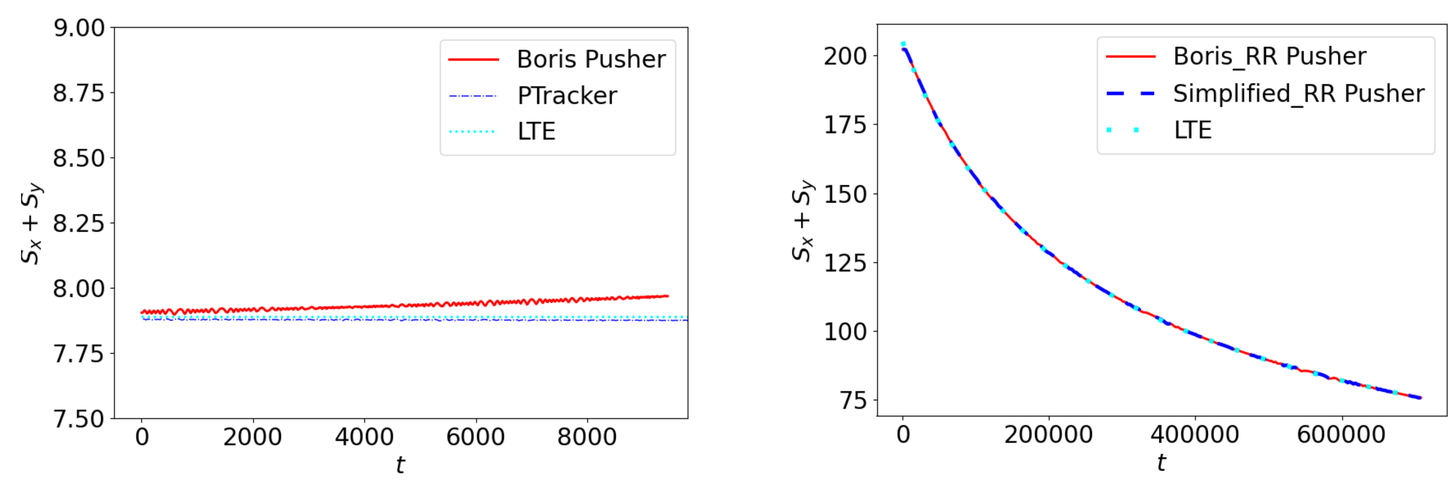

(a) (b)

Figure 3. Area in transverse phase space (S_x+ S_y) changing with time: (a) In the betatron phase shift dominant regime, comparison among Boris Pusher, Ptracker [2] and long-term evolution equation (LTE) [3]; (b) In the radiation reaction dominant regime, comparison among Boris_RR Pusher, Simplified_RR Pusher, and Long-Term Evolutionary Equation (LTE) [3].

Conclusion:

1. A three-dimensional betatron oscillation model is established; Long-term equations give information on amplitude, phase and average energy changing with time;
2. Simulation based on three-dimensional betatron oscillation model can be done by five particle pushers;
3. When $k_p r_e\langle\gamma\rangle^{5/2} \ll 1$, the precession movement of the elliptical betatron trajectory is observed, and the angular velocity of precession is consistent with theoretical expectations;
4. When $k_p r_e\langle\gamma\rangle^{5/2} \gg 1$, RR reduces the area in transverse phase space and makes the ellipse become thinner.

E-mail: liuyulong@ihep.ac.cn

A Method to Establish Height Datum Online Based on Absolute Hydrostatic Leveling System

MA NA[1,2], JIN WEIQI[1], DONG LAN[2], Wang TONG[2], LI BO[2]

1. Key Laboratory of Optoelectronic Imaging Technology and System, Beijing University of Technology
2. Spallation Neutron Source Science Center

Introduciton

With the increase of the scale and energy of the accelerator, more requirements are put forward for alignment. This paper proposes Absolute Hydrostatic Leveling System (AHLS), for establishing height datum . The principle of AHLS is described in detail, and it is emphasized that absolute calibration of the level is crucial for implementing this plan. A set of absolute calibration methods for non-contact absolute hydrostatic level is proposed, including measuring key dimensions of the level and liquid depth. The absolute calibration accuracy reaches 0.031mm. The height accuracy of validating an AHLS between two points within 10 meters using a laser tracker is more than 0.05mm. The results demonstrate the feasibility of using AHLS to establish absolute height datum with high precision. With this method, the absolute height of each point can be obtained independently without any accumulated errors, allowing the establishment of height datum with high precision on a large scale. This approach can be used in the next generation of accelerator devices and also represents a novel method for achieving high-precision vertical monitoring.

New Method
Absolute Hydrostatic Level System(AHLS)

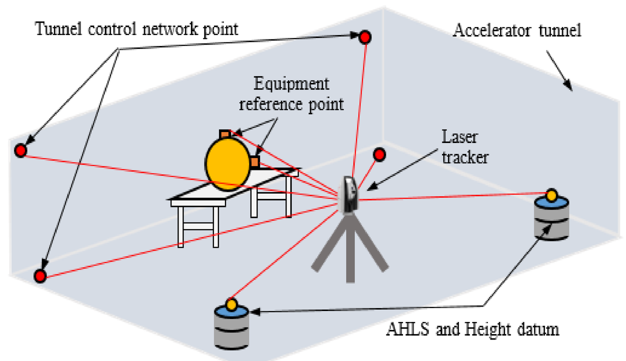

AHLS uses the actual level surface within the HLS as a datum, with no accumulation of errors in the system, allow for obtaining high-precision absolute height of leveling points, online and in real-time. The height can be used not only to establish a high-precision height datum for the overall device in combination with leveling, but also as a high-precision height datum point in the tunnel to align critical devices .This is a new method for creating high-precision absolute height datum.

The top centre of all the levels in the figure are set with a datum base for a tracker's target ball. Using the liquid level in the system as the height datum, the absolute height (H_{i_k}) of the level is the distance from the centre of the ball to the liquid surface, and can be calculated as:

$$H_{i\_k} = A_k + (R_{i\_k} + C_k), k = 1, 2, \dots, K$$

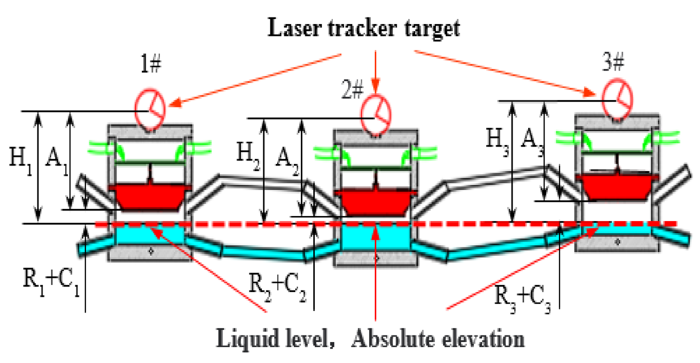

Schematic diagram of AHLS

If the values of A_k and C_k are obtained, H_{i_k} transmitted by the kth level without error at time i can be determined.

New Method
Structure of the Absolute Hydrostatic Level (AHL)

AHL is no-contact type and uses a capacitive sensor with monopole plate to monitor changes in liquid level, with a relative monitoring accuracy of 5μm. The structure and components are shown in Figure. This level is designed with a 1.5-inch datum base for tracker's target ball at the top centre, allowing for absolute calibration of liquid level extraction. This level can not only use the absolute height obtained by monitoring the ground settlement as height datum for height adjustment, improving the absolute accuracy of the overall device's height, but also serve as a datum point for high-precision adjustment of the nearby device's height, achieving high-precision alignment of critical devices.

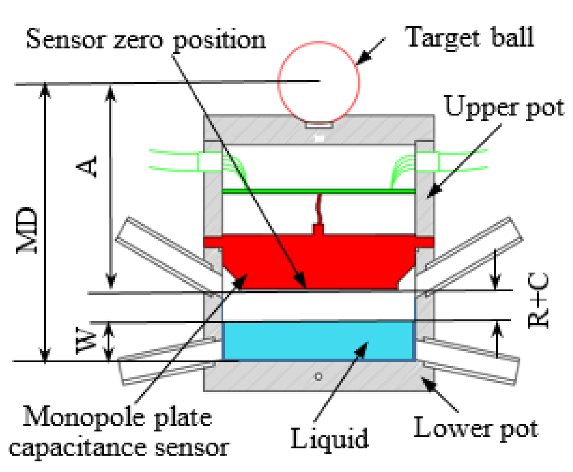

Non-contact capacitive level

New Method
Absolute Calibration of the Level(1)

The absolute calibration of the level is crucial for implement AHLS, the accuracy of the height obtained by AHLS depends on the precise determination of the constant C_k and absolute calibration value A_k of each level.

$$A_k = MD_k - W_k - (R_k + C_k)$$

The three key parameters of absolute calibration for AHL, include the distance MD_k from the bottom of the lower bowl to the centre of the target ball, the liquid depth W_k, and the absolute distance $R_k + C_k$ from the zero position of the sensor to the liquid surface.

- MD of the bowl was measured by the three-coordinate measuring machine (CMM),
- the reading R_k of the level was recorded directly and repeated several times.
- Absolute measurement of the liquid depth W_k based on the coaxial displacement meter

Absolute Calibration of the Level(2)

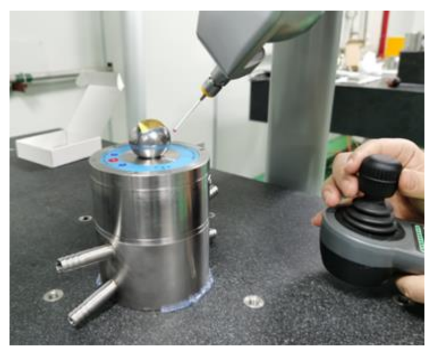

MD measured by CMM

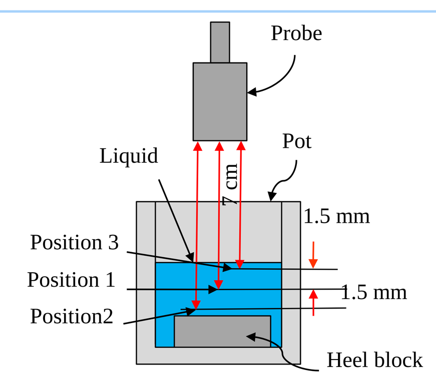

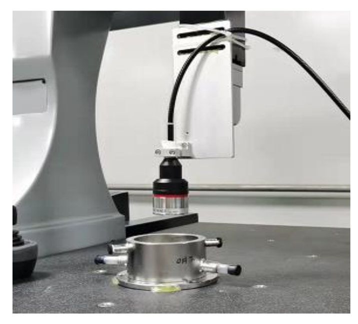

Liquid depth W_k based on the coaxial displacement meter

The accuracy of absolute calibration value A_k can be calculated as:

$$m_A = \sqrt{{m_{MD}}^2 + {m_W}^2 + {m_R}^2}$$

The measurement accuracy m_{MD} of the bowl structure was 5μm, the measurement accuracy m_W of the liquid depth was 0.03mm, and the reading accuracy m_R of AHL was 5μm. The absolute calibration accuracy m_A of the level was within 0.031mm.

Verification and discussion

The absolute height of level K at time i is calculated as:

$$H_{i_k} == MD_k - W_k - (R_k + C_k) + (R_{i_k} + C_k) = MD_k - W_k - R_k + R_{i_k}$$

Two-point AHLS verification experiment was implemented. The accuracy was verified by comparing the absolute height difference between Level 1# and Level 2# measured by the laser tracker and two-point AHLS.

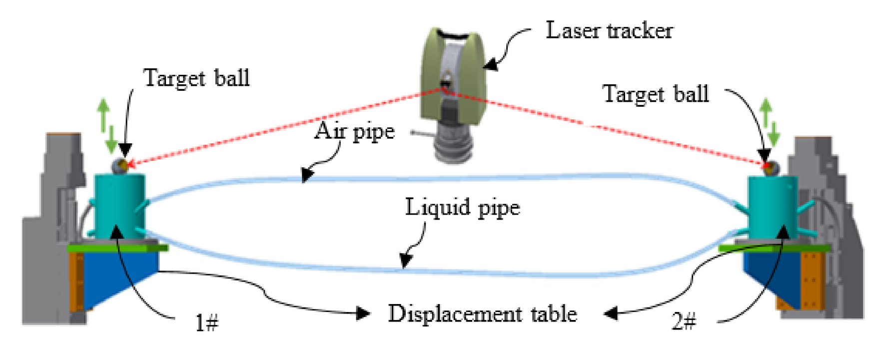

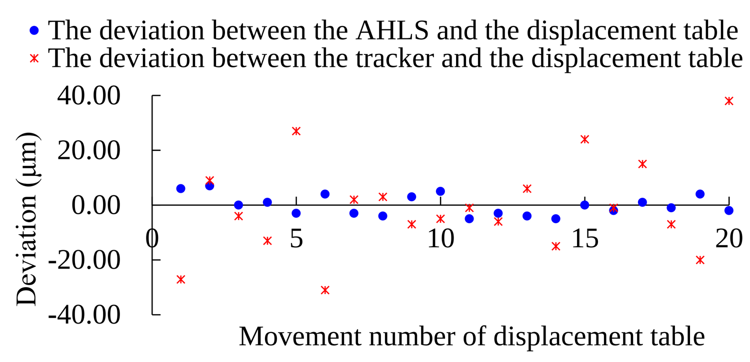

The difference between the level and displacement table ranged from -3 μm to 7 μm. After eliminating the instrumental error of the displacement table itself, the relative monitoring accuracy of the level was within 5 μm, which met the nominal accuracy of the level.

Based on the measurement results from 22 upward and downward points, the RMS of all deviations is 0.031. The experiment shows that AHLS can achieve absolute height with an accuracy of no less than 0.05mm within a 10m range, supporting the feasibility of the principle of absolute height acquisition of AHLS.

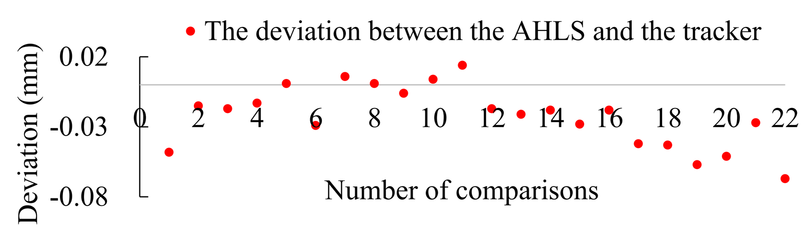

Conclusion

This paper proposes a method for establishing absolute height datum based on the accelerator settlement monitoring method HLS, called AHLS. AHLS not only provides relative monitoring, but can also provide absolute datum. The laboratory established an AHLS between two points within 10 meters and used a laser tracker with an electronic level and a micrometer displacement table to verify and calibrate the principle and absolute height accuracy of the AHLS. The results showed that the absolute height accuracy within 10 meters is not less than 0.05mm.

The 2023 International Workshop on the High Energy Circular Electron Positron Collider (CEPC2023), Nanjing, China, Oct 23-27, 2023

Preliminary design of energy recovery scheme for high-power klystron*

Yu Liu[1], Zusheng Zhou†[1], Ouzheng Xiao, Yiao Wang[1], Yunlong Chi, Fei Li,
Munawar Iqbal, Abid Aleem, Han Xiao[1], Wenbing Gao[1], Noman Habib[1]
Institute of High Energy Physics, Chinese Academy of Sciences, Beijing 100049, China
[1]also at University of Chinese Academy of Sciences, Beijing 100049, China
中國科學院高能物理研究所
Institute of High Energy Physics
Chinese Academy of Sciences

Based on the high efficiency klystron scheme of circular electron positron collider (CEPC), the depressed collector design is proposed to improve the overall efficiency of RF power source. The depressed collector technology has been applied in low power microwave electronic vacuum devices such as TWT and TV communication klystrons. The velocity of electrons entering the klystron collector is scattered, and it is difficult to use the depressed collector to sort the velocity of electrons. This paper will carry out a detailed theoretical analysis of the depressed collector and determine its basic design scheme for CEPC high efficiency klystron. In order to verify the klystron energy recovery scheme, an energy recovery verification device is designed. DGUN and CST codes are used for design optimization of verification device beam. ANSYS thermal analysis is carried out on the depressed collector to determine the electron gun and depressed collector design scheme. The verification device is expected to be completed by the end of the year to carry out high-power experiments.

INTRODUCTION

The depressed collector is an important method to improve the efficiency of microwave tubes by recovering the energy of waste electrons. This technology has been widely used in TWT, and its collector recovery efficiency is more than 70%. Figure 1 shows the basic principle of an energy recovery device. At present, the application of depressed collector on klystron is mainly used in low power klystron for TV and communication, but there is little research on depressed collector technology on high power klystron. The characteristics of klystron bring some difficulties to the design of depressed collector. The proposal of depressed accelerator puts forward higher demand for high power klystron efficiency. The application of depressed collector technology in high power klystron further improves the overall efficiency of power source system.In order to verify the feasibility of klystron energy recovery scheme, we have completed the design of energy recovery verification device. The design scheme and corresponding simulation results are presented.

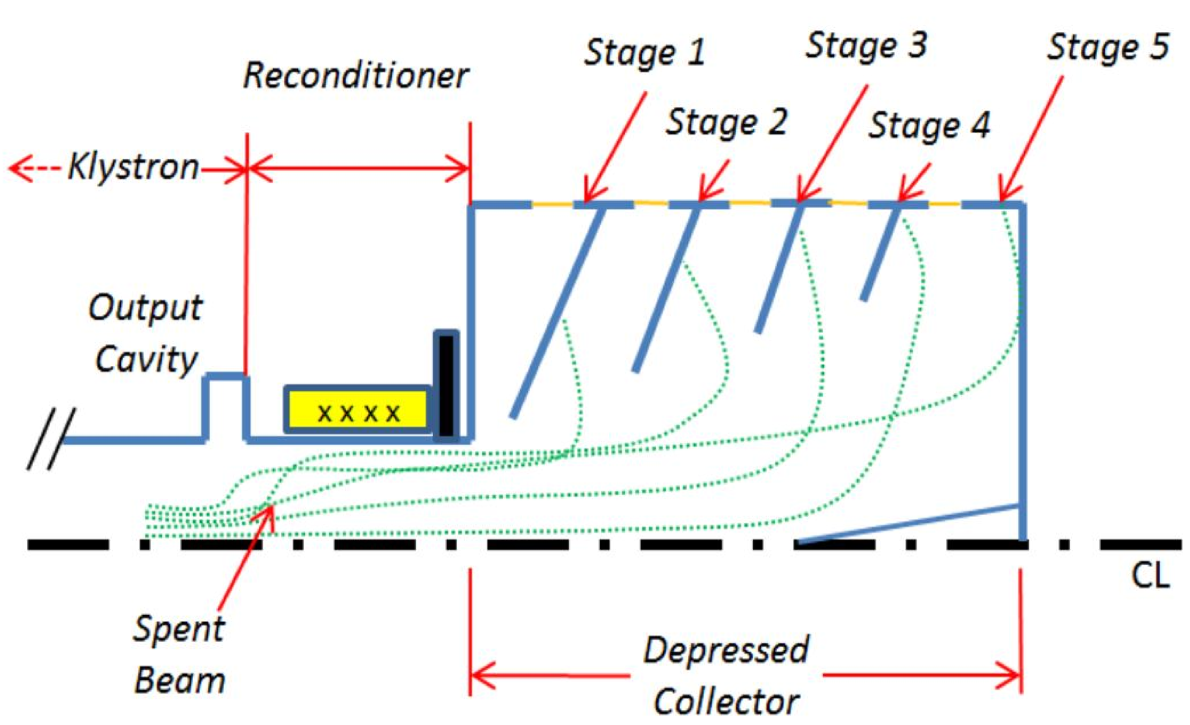

Figure 1:Depressed collector structure

DEPRESSED COLLECTOR PRINCIPLE

The recovery power of depressed collector depends on the selection of collector potential. A deceleration field is established in space by providing the collector with a lower potential than the tube body, after which the waste electrons are decelerated by the electric field upon entering the collector. The efficiency of the klystron is improved by the energy recovery on the electrode, and the heat dissipation pressure of the collector is also reduced.

Based on the high efficiency klystron of CEPC, the depressed collector scheme is designed. The high efficiency klystron has a saturated output power of 800kW and a design efficiency of more than 75%. The main design parameters of the high-efficiency klystron are shown in Table 1.

Table 1: High efficiency klystron parameters of CEPC

Operating frequency	650 MHz
Output power	≥800 KW
Beam voltage	113 kV
Beam current	9.5 A
Beam perveance	0.25 μP
Efficiency	≥75%

Due to the need of low-level feedback control, the klystron usually works in the approximately linear region, and its output power is based on 700 kW. The probability distribution of its energy entering the collector pole waste electron is shown in Figure 2.

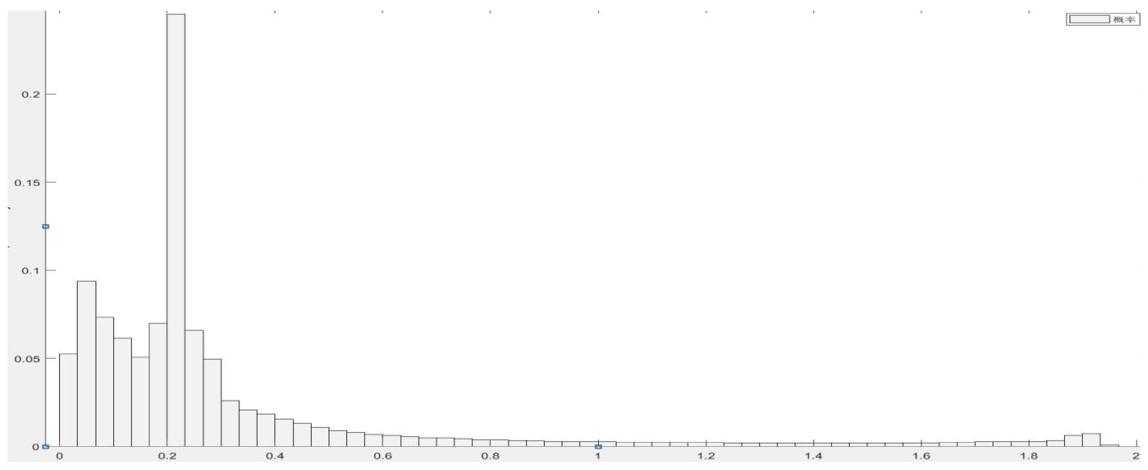

Figure 2 Energy distribution of Klyc waste electrons

The following formula is used to obtain the recovery power of the multi-stage depressed collector :

$$P_{rec} = \sum_{1}^{N-1} \int_{Vi}^{Vi+1} J_{waste}(V) I_0 V_i dV + \int_{V_N}^{\infty} J_{waste}(V) I_0 V_N dV$$

DESIGN OF VERIFICATION DEVICE

Before processing the depressed collector klystron, we use the energy recovery verification device to verify the key technology. The basic structure of the verification device is shown in Figure 3.

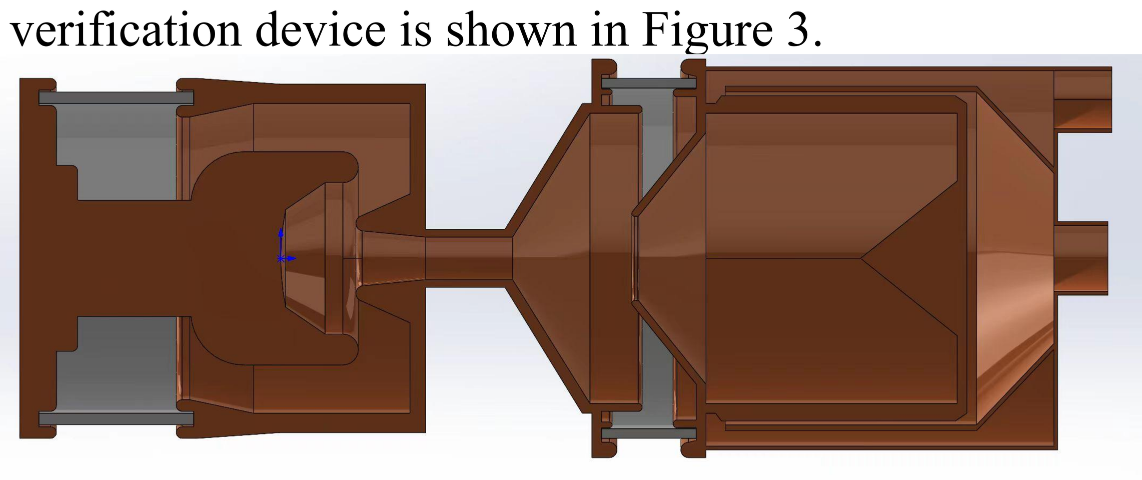

Figure 3:Structure of the device

Based on the CEPC high efficiency klystron single-pole depressed collector parameter, the electron gun voltage is 30kV, the current is 4.5A, and the depressed collector voltage is 27kV. Figure 4 shows the results of the gun in DGUN and CST. The depressed collector adopts axisymmetric structure, as shown in Figure 5. The structure has two electrodes, the first electrode is consistent with the potential of the tube, and the second electrode applies a negative high voltage to slow down the electrons and to recover energy. In the case of considering secondary electrons, the waste electron reflux rate is low, and the results meet the requirements.

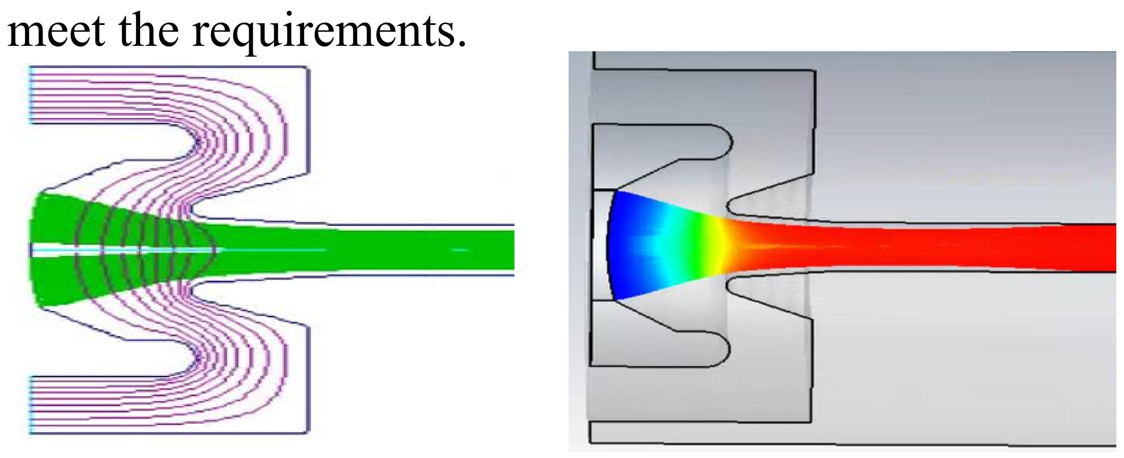

Figure 4: Beam optic simulation results in DGUN and CST

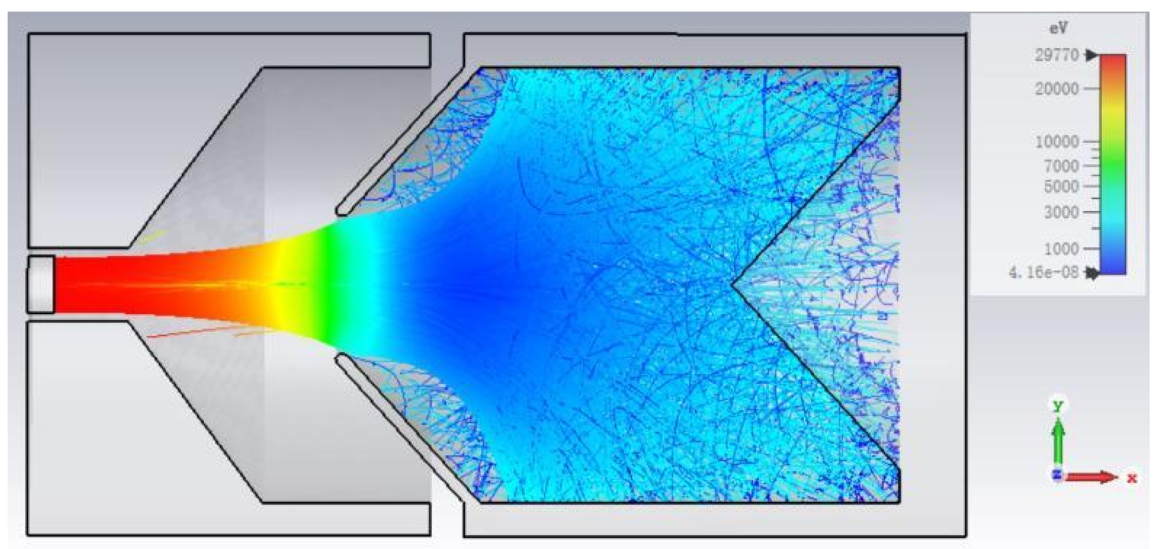

Figure 5 Electron trajectory in the collector

THERMAL SIMULATION

The structural model was established in ANSYS, and the grid was divided when the calculation accuracy was met. Thermal load was added to the model, boundary conditions (ambient temperature 293K) and heat transfer mode were set, and thermal analysis was carried out using ANSYS Workbench module. Figure 4 shows the temperature distribution on the collector section, with a maximum temperature of 363K. The results can provide reference for the next water cooling design.

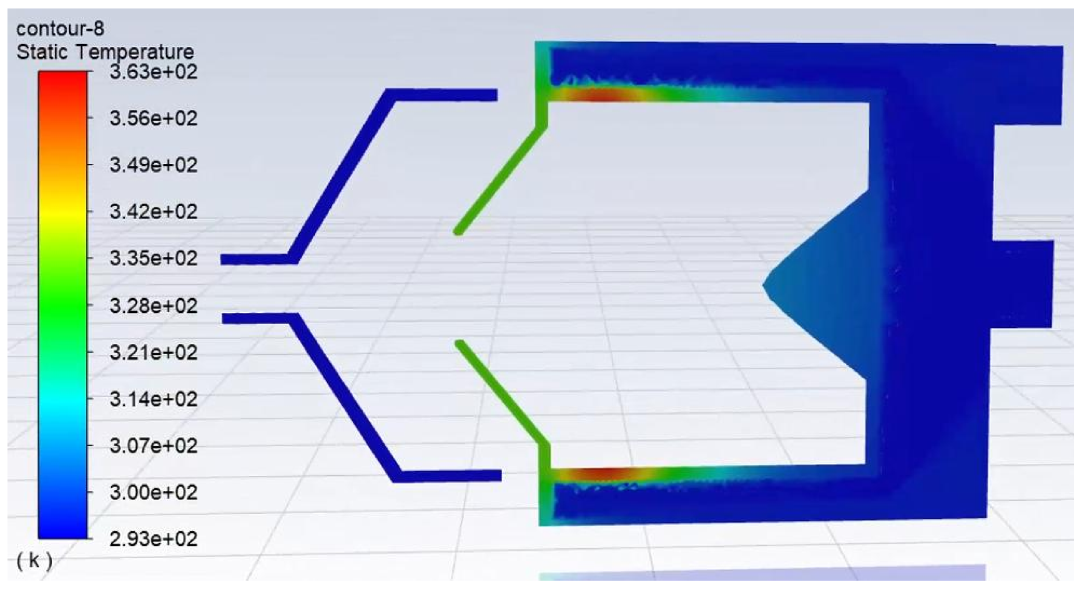

Figure 4:Collector temperature distribution by ANSYS

SUMMARY AND OUTLOOK

In this paper, we take the high efficiency CEPC klystron as a research object. The depressed collector is theoretically analyzed, and the electrode parameters are determined. In order to verify the key technology of energy recovery klystron, we designed an energy recovery verification device composed of gun and collector. The beam optics were simulated in DGUN and CST, and thermal analysis of the collector was performed using ANSYS. The structural design of gun and collector is completed. The simulation results show that the electron trajectory and thermal analysis of the collector meet the design requirements.

REFERENCES

[1]Kosmahl H G. Modern multistage depressed collectors—A review[J]. Proceedings of the IEEE, 1982, 70(11): 1325-1334.
[2]DAYTON J A. System efficiency of a microwave power tube with a multistage depressed collector(Current distribution estimates for microwave power tube with depressed multistage collector)[J]. 1972.
[3]Jiang Y, Teryaev V E, Hirshfield J L. Partially grounded depressed beam collector[J]. IEEE Transactions on Electron Devices, 2015, 62(12): 4265-4270.
[4]Vaughan J R M. Synthesis of the Pierce gun[J]. IEEE Transactions on Electron Devices, 1981, 28(1): 37-41.
[5]Hamme F, Becker U, Hammes P. Simulation of secondary electron emission with CST PARTICLE STUDIOTM[C]//Proc. ICAP. 2006: 160-163.

* Work supported by Dr. Yifang Wang's Science Studio of the Thousand Talents Project
† email address: zhouzs@ihep.ac.cn

Automatic optimization design of klystron magnetic focusing system

Y. A. Wang[1,2], Z. S. Zhou[1,2], O. Z. Xiao[1], Y. Liu[1,2], C. M[1,2]

[1]Institute of High Energy Physics, Chinese Academy of Sciences, Beijing 100049, China

[2]University of Chinese Academy of Sciences, Beijing 100049, China

Abstract

This paper introduces the development of an automatic optimization program for the magnetic focusing system of a 65MW klystron, using a multi-objective genetic algorithm. The program utilizes Poisson's magnetic field calculation software, DGUN beam optics software, and Python data analysis software. By optimizing the beam fluctuation rate and electron beam radius, as well as adjusting the structural parameters and coil current parameters of the focusing system, the program enables efficient automatic optimization of the klystron's magnetic focusing system.

Background

In the design of the klystron's magnetic focusing system, aligning the electron beam with the magnetic field is crucial for optimal performance. Electromagnetic focusing, achieved through coil currents, allows for easy magnetic field adjustment. The design process involves optimizing the focusing coil structure and currents to determine the ideal magnetic field distribution along the klystron's axis based on electron gun parameters and beam envelope distribution. However, the simultaneous optimization of multiple coil structures and current parameters poses a challenge in the calculation process.

Methods

- Based on the parameters of the klystron electron gun, the magnetic field distribution for focusing is determined. Considering the power consumption and efficiency of the magnetic focusing system, appropriate coil sizes, quantities, and coil current values are selected.
- The relationship between individual coil current values and the overall magnetic field is analyzed, starting from the selection of coil quantities and values. Poisson's magnetic field calculation software and DGUN beam optics software, along with a multi-objective genetic algorithm in Python, are used to optimize the magnetic field and determine the desired current values for the focusing magnetic field.

Process

- **Objective function:** The multi-objective genetic algorithm is commonly used for non-linear problem-solving, mimicking natural selection and evolution. It is suitable for optimizing the complex magnetic focusing system of the klystron, where the number of coils and current values have a non-linear relationship with beam fluctuation rate and fill factor.
- **Relationship equation:** Coil quantity and current values are variables in the klystron's magnetic focusing system. Python uses Poisson and DGUN software to analyze magnetic field and beam characteristics. A multi-objective genetic algorithm optimizes coil current values for desired beam performance, while ensuring satisfactory fill factor.

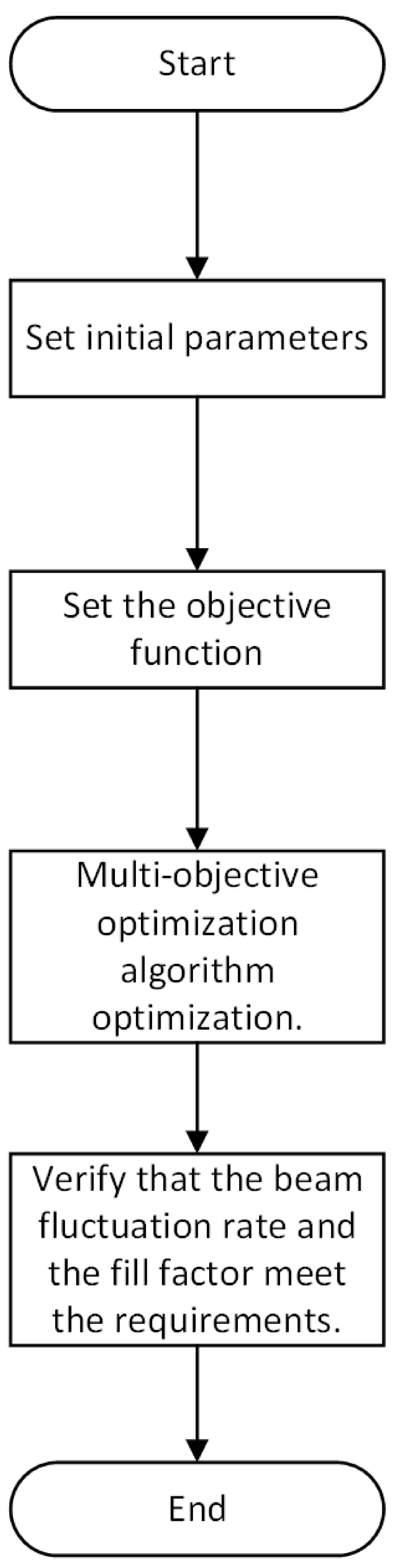

Figure 1(a) Overall Optimization Program Flowchart

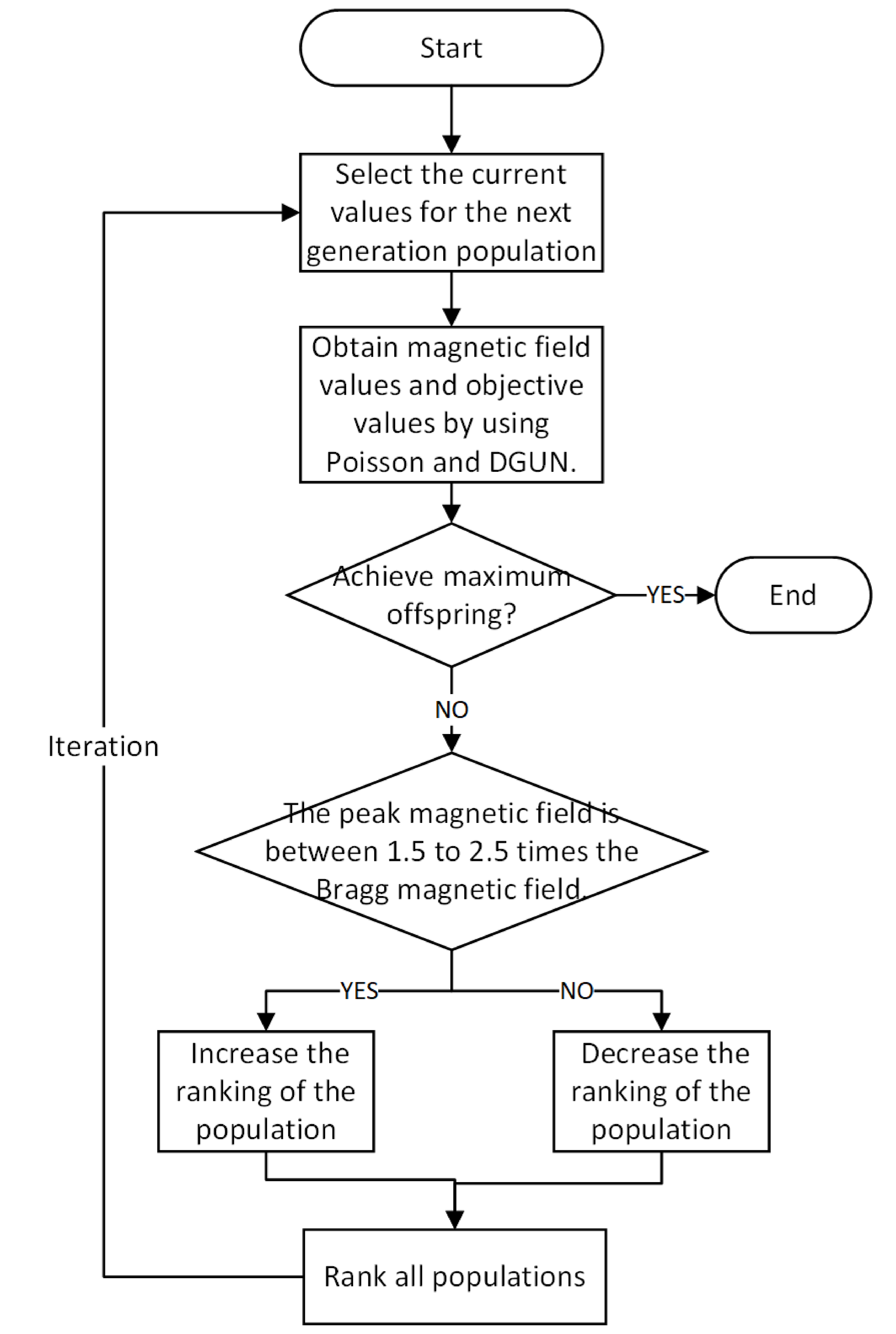

Figure 1(b) Multi-objective Optimization Program Flowchart

Practical Example

- To validate the effectiveness of the algorithm, this study applies it to optimize the magnetic focusing system of a domestic 65MW klystron. The optimization is conducted with the objectives of minimizing beam fluctuation and maximizing the fill factor, by optimizing the current values for different numbers of coils.

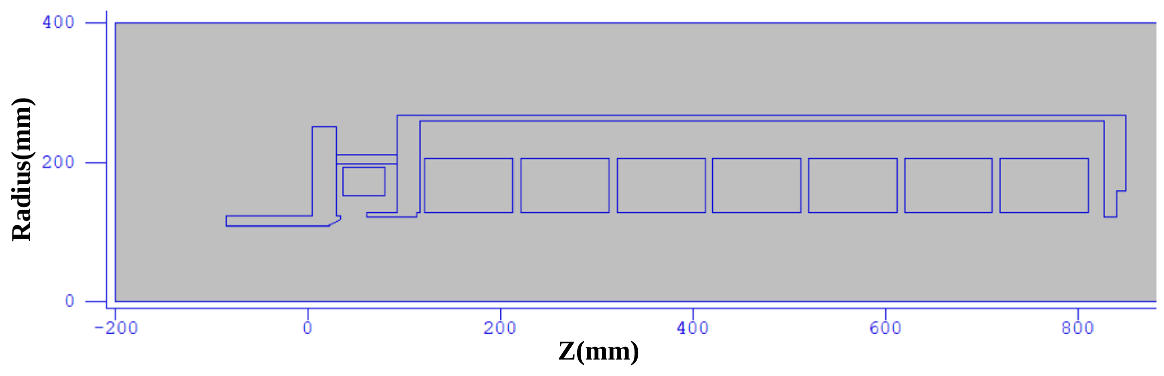

Figure 2 Schematic of klystron focusing system structure

- Specifically, the study considers the cases of 4,8 and 16 coils, with a schematic diagram of the coil structure (8 coils) shown in Figure 2. A popular size of 100 and 60 iterations are set for the optimization process. The optimization results for the current values under different numbers of coil are shown in Figure 1, with the blue data representing the optimization results for 4 coils the orange data for 8 coils, and the green data for 16 coils. The comparison of the optimal current values for the two objectives is shown in Figure 5.

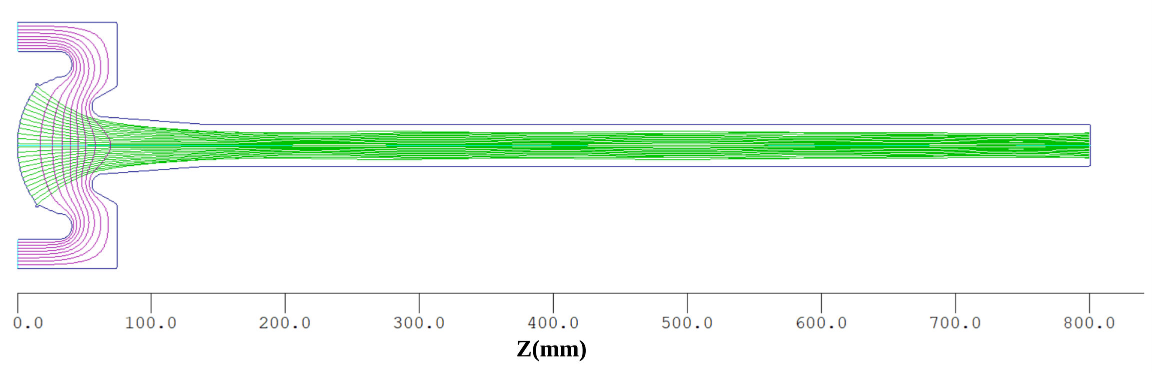

Figure 3 DGUN beam optics for 16 coil structures

From Figure 4, increasing the number of coils from 4 to 8 slightly reduces the beam fluctuation rate. Further increasing it to 16 significantly reduces the beam fluctuation rate. Figure 5 shows the magnetic field distribution for different coil configurations. In the rising region, the magnetic field similarity is high among the configurations. However, in the uniform region, 8 coils have better magnetic field uniformity than 4 coils, and 16 coils have even better uniformity. The optimal beam fluctuation rates are 8.5% for 4 coils, 5.6% for 8 coils, and 3.8% for 16 coils. Increasing the number of coils gradually decreases the beam fluctuation rate. Figure 3 illustrates the beam optics for the configuration with 16 coils.

Increasing the number of coils facilitates adjusting the focusing magnetic field, but excessive coils can increase costs. The final selection of the number of coils will consider meeting the beam fluctuation rate and fill factor requirements, as well as cost and processing difficulty.

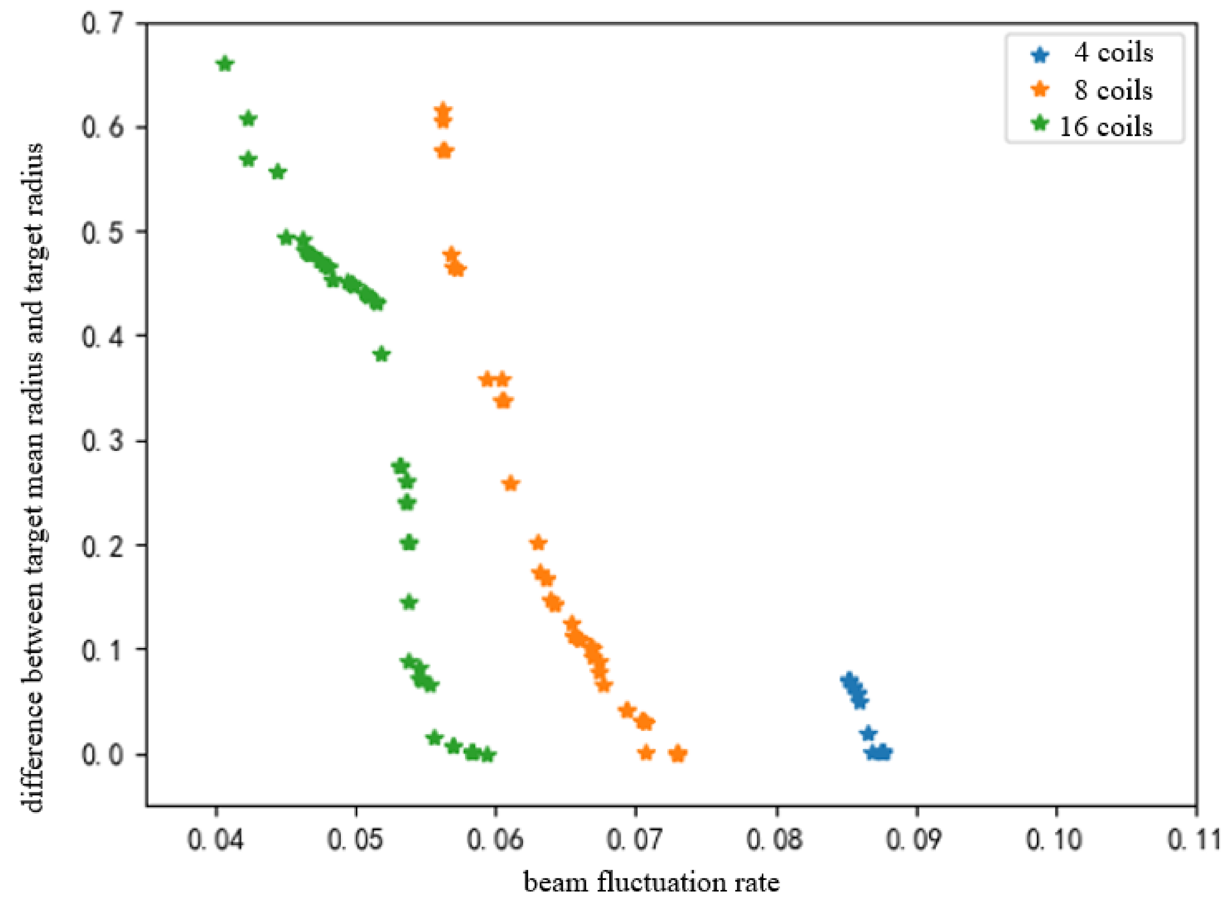

Figure 4 Distribution of 3 coil structures target values

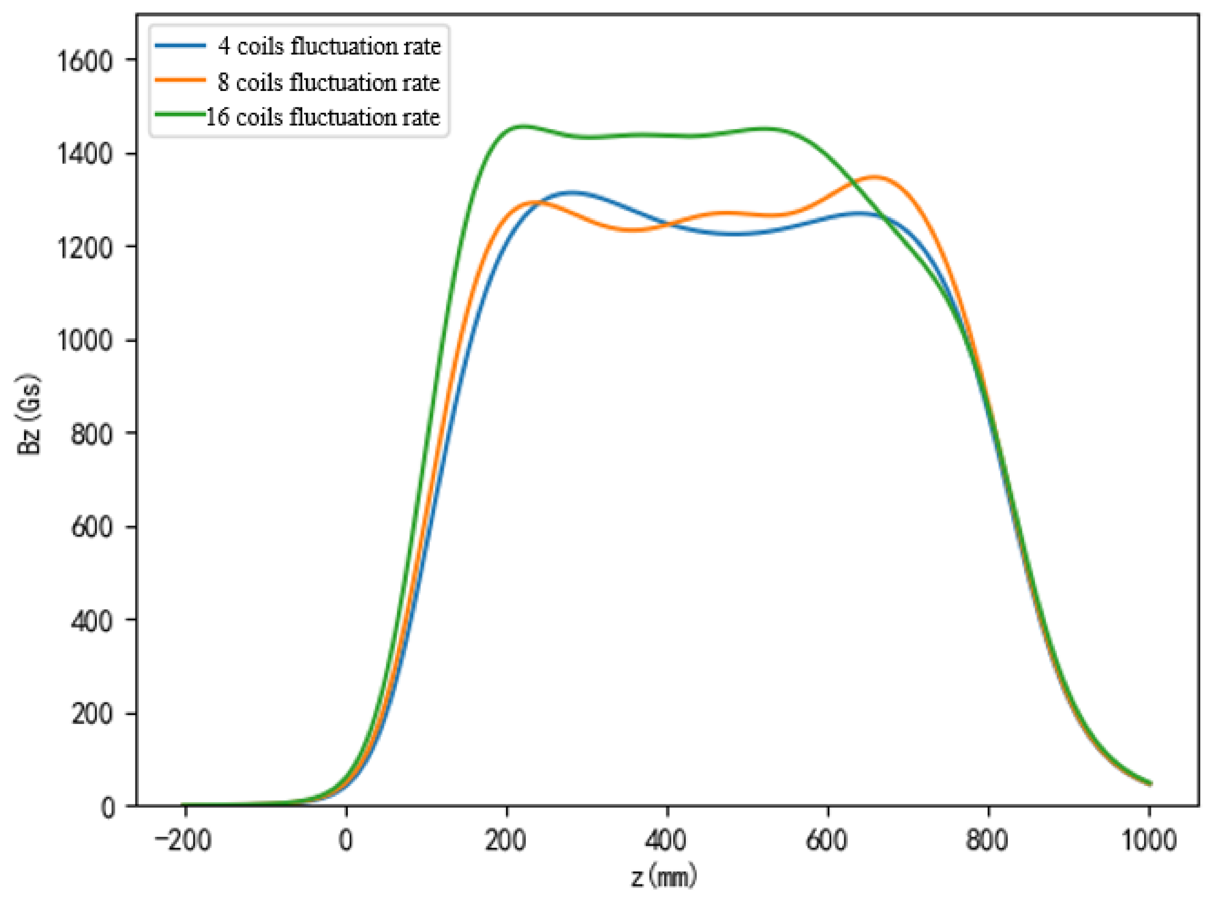

Figure 5 Magnetic field values of 3 coil structures

Conclusion

This paper investigates the 65MW domestic klystron magnetic focusing system and develops an optimization algorithm for its coil structures. It analyzes the impact of different coil quantities on magnetic field distribution and determines coil structures and current values that meet beam dynamics requirements. The optimization program significantly improves design efficiency.

References

[1] Kornyukhin G A , Kulipanov G N , Litvinenko V N ,et al.The magnetic system of an optical klystron using SmCo permanent magnets[J].Nuclear Instruments and Methods in Physics Research, 1983, 208(1-3):189-191.DOI:10.1016/0167-5087(83)91123-7.

[2] Morev S , Komarov D , Muraviev E ,et al.Estimation of the Focusing Magnetic Field in High-power Multibeam Klystrons with Electron Beam Dynamic Defocusing Factor[C]//2020 International Conference on Actual Problems of Electron Devices Engineering (APEDE).2020.DOI:10.1109/APEDE48864.2020.9255526.

[3] Akimov P I , Nikitin A P , Melnichuk G V ,et al.Particularities of reversible magnetic focusing system development for multi-beams klystrons[C]//Vacuum Electronics Conference.IEEE, 2013:1-2.DOI:10.1109/IVEC.2013.6571033.

[4] Elmowla K M M G , Chai J S , Yeon Y H ,et al.An efficient simulation method of a cyclotron sector-focusing magnet using 2D Poisson code - ScienceDirect[J].Nuclear Inst & Methods in Physics Research A, 2016, 832:95-102.DOI:10.1016/j.nima.2016.04.101.

[5] B M I A , C Z Z A , A O X ,et al.Design, simulation and analysis of beam optics and solenoid of high-power gun for RF power source[J].Nuclear Instruments and Methods in Physics Research Section A: Accelerators, Spectrometers, Detectors and Associated Equipment, 2021.[6]Rossum, Drake G V , Jr F L .Python language reference manual[J].Manual Network Theory Ltd, 2003.

[6] K. Deb, A. Pratap, S. Agarwal and T. Meyarivan, "A fast and elitist multiobjective genetic algorithm: NSGA-II," in IEEE Transactions on Evolutionary Computation, vol. 6, no. 2, pp. 182-197, April 2002, doi: 10.1109/4235.996017.

* Work supported by Dr. Yifang Wang's Science Studio of the Thousand Talents Project

† email address: zhouzs@ihep.ac.cn wangya@ihep.ac.cn

The 2023 International Workshop on the High Energy Circular Electron-Positron Collider
Oct 23-27, 2023, Nanjing, China

Studies of LWFA-driven PWFA Hybrid Acceleration

Xinyuan Chang[1,2], Ming Zeng[2], Jia Wang[1,2], Dazhang Li[2]

[1] University of Chinese Academy of Sciences, School of Physical Sciences, Beijing 101408, China
[2] Institute of High Energy Physics, Chinese Academy of Sciences, Accelerator Division, Beijing 100049, China

Introduction

The plasma-based acceleration (PBA) has acceleration gradients exceeding those in conventional acceleration by several orders of magnitude[1]. The beam-driven plasma wakefield acceleration (PWFA) offers acceleration gradients of 1-100 GeV/m. Compared to the laser-driven plasma wakefield acceleration (LWFA), it achieves higher single-stage energy gain. However, the availability of PWFA driven by linear accelerators is limited, posing a constraint on the widespread implementation of this technology. LWFA is more feasible due to the better accessibility of lasers and is capable of generating femtosecond-scale GeV electron bunches with peak currents exceeding 10 kA which can serve as ideal electron bunches for PWFA.

To investigate the LWFA-driven PWFA hybrid acceleration process we proposed, we use the Fourier-Bessel Particle-in-Cell (FBPIC) algorithm in particle simulations. In the LWFA stage, we utilize two ultra-intense lasers (both normalized vector potentials $a_0 > 3$) to trigger two ionization injections of electron bunches in mixed gaseous targets. These two electron bunches are subsequently used for the PWFA stage to sustain the acceleration process. This scenario is illustrated in Fig. 1.

Through our simulation studies, we observe the entire acceleration process and consider the feasibility of this LWFA-driven PWFA hybrid acceleration process.

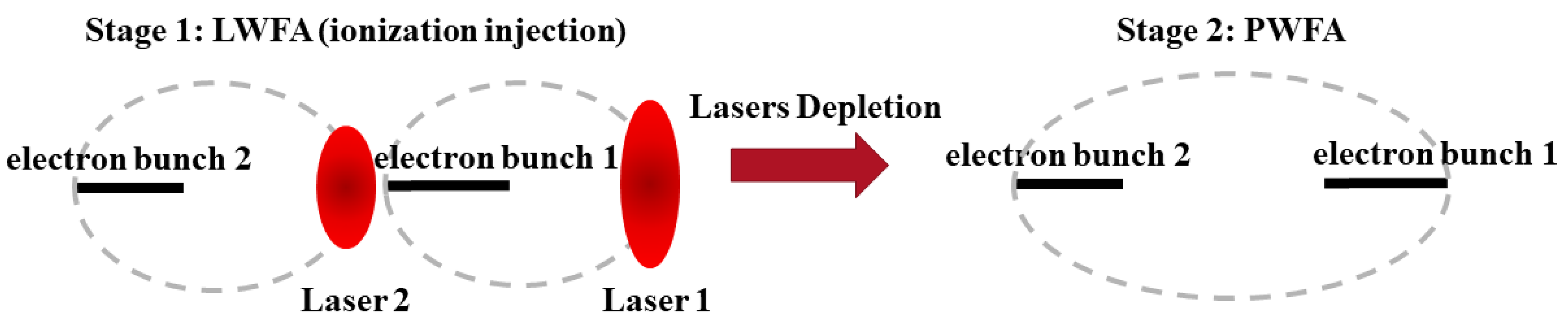

FIG. 1. Illustration on LWFA-driven PWFA hybrid acceleration.

Simulation Setup

1. Ionization injection

Ionization-induced injection in mixed gaseous targets has been considered as an effective scheme to gain high charge electron bunches. This mechanism is based on two processes: pre-ionization and ionization.

Pre-ionization means at least one gas element in the mixed gaseous targets should have a relatively low ionization threshold and can be pre-ionized and acted as background plasma, and ionization means this gas element should have inner shells with higher ionization thresholds such that the laser with sufficiently high intensity can release these inner shell electrons which will be trapped and accelerated in the wake[2].

2. Simulation parameters

In our hybrid acceleration scheme, we use carbon dioxide (CO_2) gas as the gaseous target, for C^{4+} and O^{6+} have large differences in ionization energy, as shown in Fig. 2(a) and Fig. 2(b).

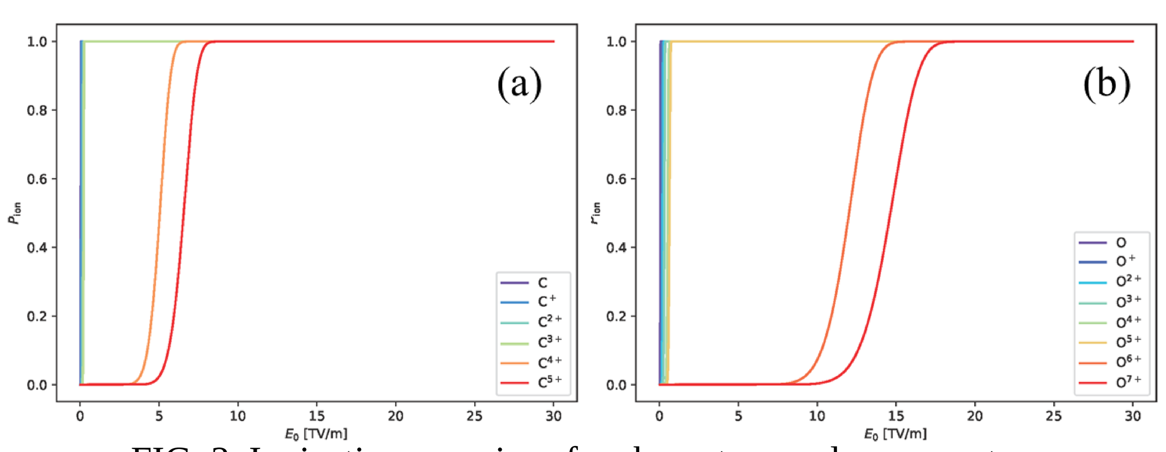

FIG. 2. Ionization energies of carbon atom and oxygen atom.

Under the assumption that the gaseous target has been fully pre-ionized by the laser pluses, we choose laser 1 to ionize the C^{4+} but not to ionize O^{6+} with electric-field intensity above 8 TV/m and below 19 TV/m, while laser 2 to ionize O^{6+} with electric-field intensity above 19 TV/m. Detailed laser parameters are shown in Table. 1.

TABLE 1. Laser parameters

	λ_0	a_0	w_0	τ_{FWHM}
Laser 1	0.8 μm	3.5	11 μm	20 fs
Laser 2	0.4 μm	4.0	4 μm	10 fs

Results and Conclusion

We choose the carbon dioxide gas density $n_{CO_2} = 1 \times 10^{17}\text{cm}^{-3}$ such that the density of C^{4+} is $n_{C^{4+}} = 1 \times 10^{17}\text{cm}^{-3}$, the density of O^{6+} is $n_{O^{6+}} = 2 \times 10^{17}\text{cm}^{-3}$, the pre-ionized background plasma density is $n_e = 1.6 \times 10^{18}\text{cm}^{-3}$. From our simulation studies, we have observed two different acceleration stages:

1. LWFA stage

The two lasers can trigger ionization injections of two electron bunches in LWFA stage.

The injection of the first electron bunch is shown in Fig. 3. Fig. 3(a) is the snapshot in the y-z slice, Fig. 3(b) is the z-direction momentum distribution. Detailed bunch parameters are shown in Table. 2.

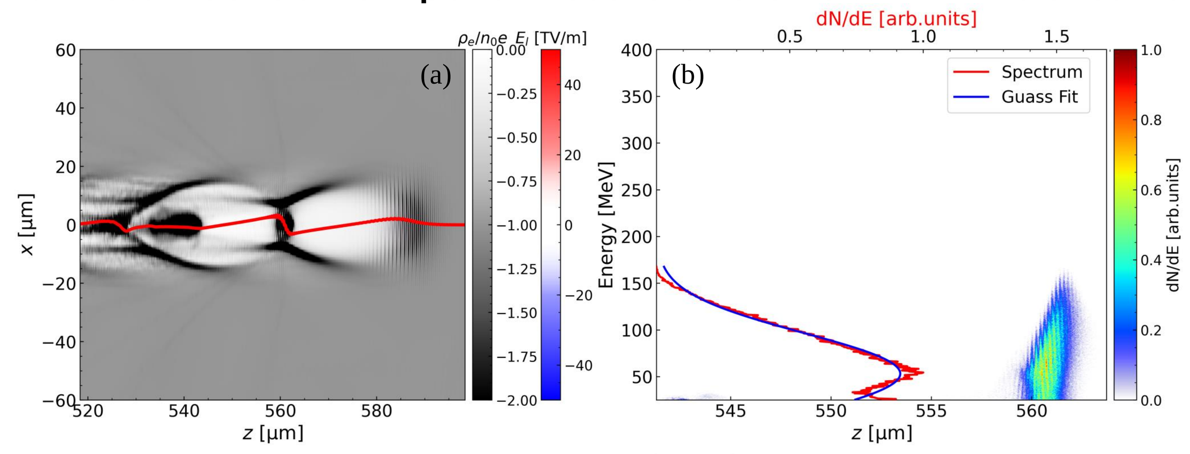

FIG. 3. The injection process of the first electron bunch.

TABLE 2. First electron bunch parameters

Charge (>25 MeV)	center energy	energy spread	emittance (x-direction)	emittance (y-direction)
280.05 pC	53.23 MeV	102.22 MeV	8.54 mm mrad	1.54 mm mrad

The injection of the second electron bunch is shown in Fig. 4. Fig. 4(a) is the snapshot in the y-z slice, Fig. 4(b) is the z-direction momentum distribution. Detailed bunch parameters are shown in Table. 3

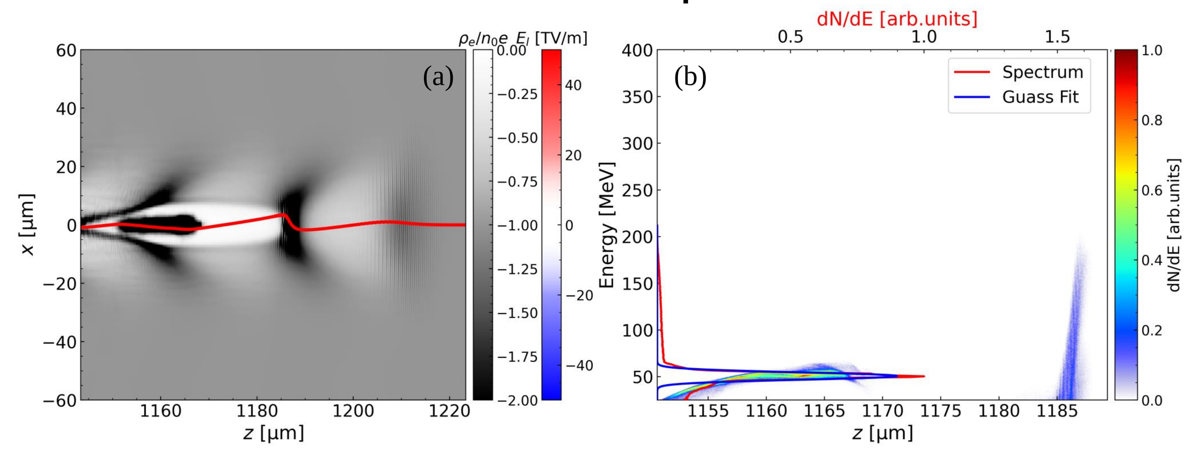

FIG. 4. The injection process of the second electron bunch.

TABLE 3. Second electron bunch parameters

charge (>25 MeV)	center energy	relative energy spread	emittance (x-direction)	emittance (y-direction)
550.60 pC	50.72 MeV	18.08 %	11.04 mm mrad	3.78 mm mrad

2. PWFA stage

The two electron bunches from LWFA stage are used in PWFA stage to sustain acceleration process. This process is shown in Fig. 5. Fig. 5(a) is the snapshot in the y-z slice, Fig. 5(b) is the z-direction momentum distribution. Detailed bunch parameters are shown in Table. 4.

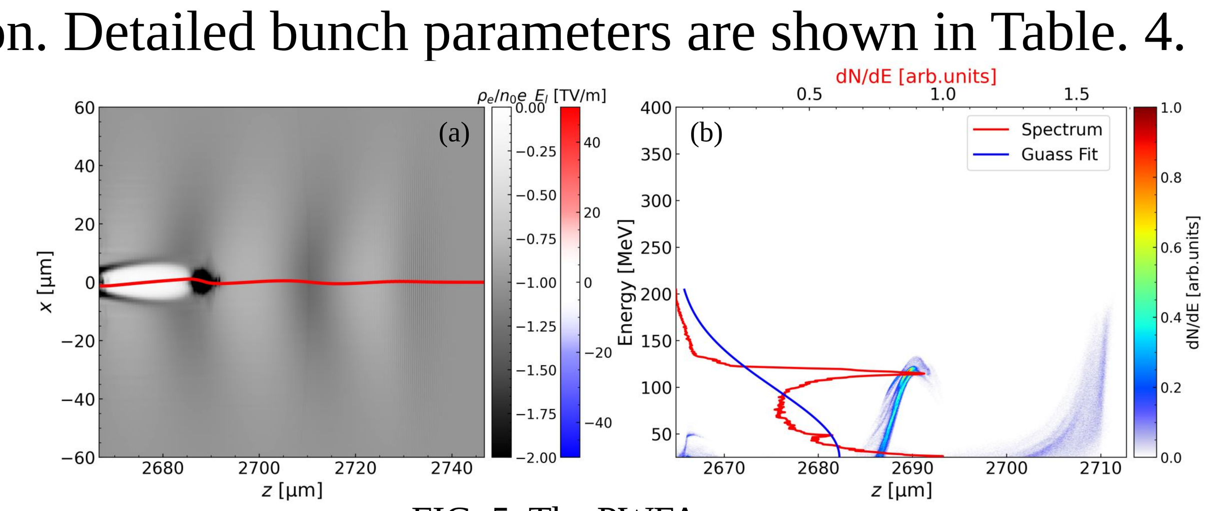

FIG. 5. The PWFA process.

TABLE 4. PWFA electron bunch parameters

charge (105 – 125 MeV)	center energy	relative energy spread	emittance (x-direction)	emittance (y-direction)
48.96 pC	114.03 MeV	13.42 %	35.4 mm mrad	9.29 mm mrad

Future Directions

We have already proved the feasibility of this LWFA-driven PWFA hybrid acceleration process.

In our future work, we will further investigate this hybrid acceleration process. We will optimize simulation parameters, such as gas distribution, gas density, laser intensity, the frequencies and spatial distribution of two lasers, etc., to improve the bunch's quality.

Email: xychang@ihep.ac.cn

[1] Tajima and J. M. Dawson, Phys. Rev. Lett. 43, 267 (1979).
[2] M. Zeng, M. Chen, L. L. Yu, W. B. Mori, Z. M. Sheng, B. Hidding, D. A. Jaroszynski, and J. Zhang, Phys. Rev. Lett. 114, 084801 (2015).

International Workshop on The High Energy Circular Electron Positron Collider
Oct. 23 - 27, 2023, Nanjing, China

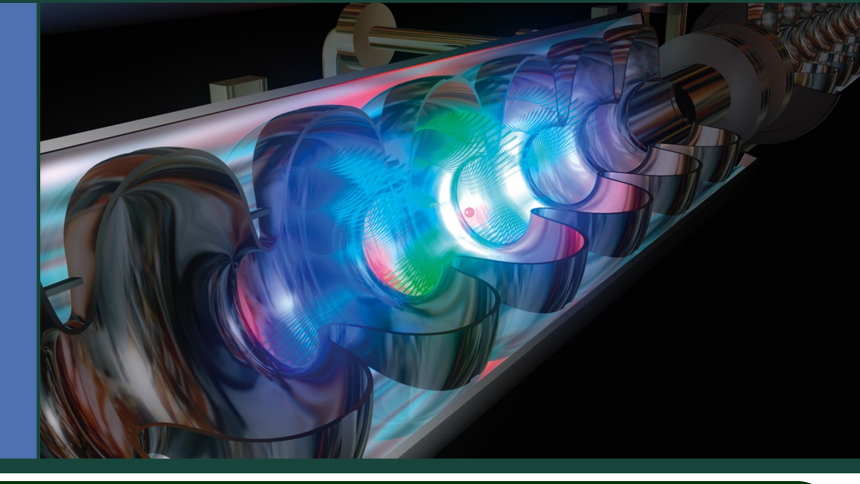

Vertical test of 650 MHz superconducting radio-frequency cavity for CEPC

Lingxi Ye, Peng Sha
Institute of High Energy Physics (IHEP), CAS

Hundreds of 650 MHz superconducting radio-frequency (SRF) cavities with high intrinsic quality factor (Q_0) and accelerating gradient (E_{acc}) will be adopted for Circular Electron Positron Collider (CEPC). The values of Q_0 and E_{acc} are obtained during vertical test at 2.0 K. Hence, high accuracy of vertical test is essential for evaluating the performance of SRF cavity. In our study, the error analysis of vertical test was conducted in the scalar case, in order to achieve high accuracy. The uncertainties of vertical test were obtained through calculation, which was approximately 3% for E_{acc} and less than 5% for Q_0. This result was reasonable and acceptable, compared with other SRF laboratories. Finally, the 650 MHz single-cell cavities for CEPC achieved state-of-the-art Q_0 and E_{acc} during the vertical tests, which exceeded 1×10^{11} and 40 MV/m, respectively.

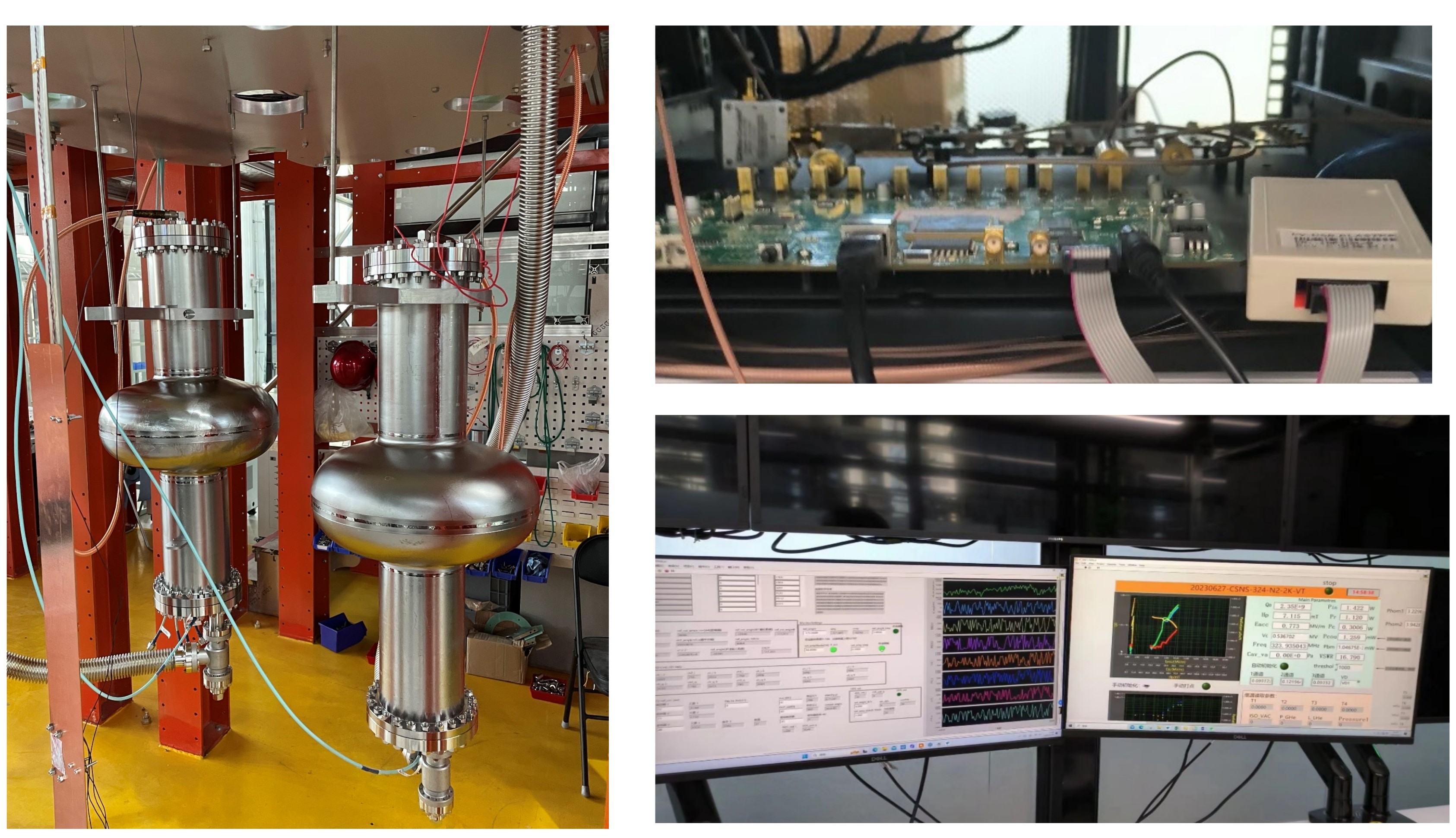

Vertical test of 650 MHz single-cell cavities for CEPC

$$Q_0 = 4\pi f \tau \frac{C_{in}P_{im} + C_\beta\sqrt{C_{in}P_{im}C_rP_{rm}}}{C_tP_{\mathrm{tm}}} \frac{C_tP'_{tm}}{C_{in}P'_{im} - C_tP'_{tm} - C_rP'_{rm}}$$

$$E_{acc} = \sqrt{4\pi f \tau \frac{C_{in}P_{im} + C_\beta\sqrt{C_{in}P_{im}C_rP_{rm}}}{C_tP_{\mathrm{tm}}} C_tP'_{tm} \frac{r/Q}{L}}$$

$$M = \begin{bmatrix} {u_{x_1}}^2 & ru_{x_1}u_{x_2} & \cdots & ru_{x_1}u_{x_n} \\ ru_{x_2}u_{x_1} & {u_{x_2}}^2 & \cdots & ru_{x_2}u_{x_n} \\ \vdots & \vdots & \ddots & \vdots \\ ru_{x_n}u_{x_1} & ru_{x_n}u_{x_2} & \cdots & {u_{x_n}}^2 \end{bmatrix}$$

$$(\delta f)^2 = \nabla f^T \cdot M \cdot \nabla f$$

Calculation of uncertainties of Q_0 and E_{acc} for vertical test

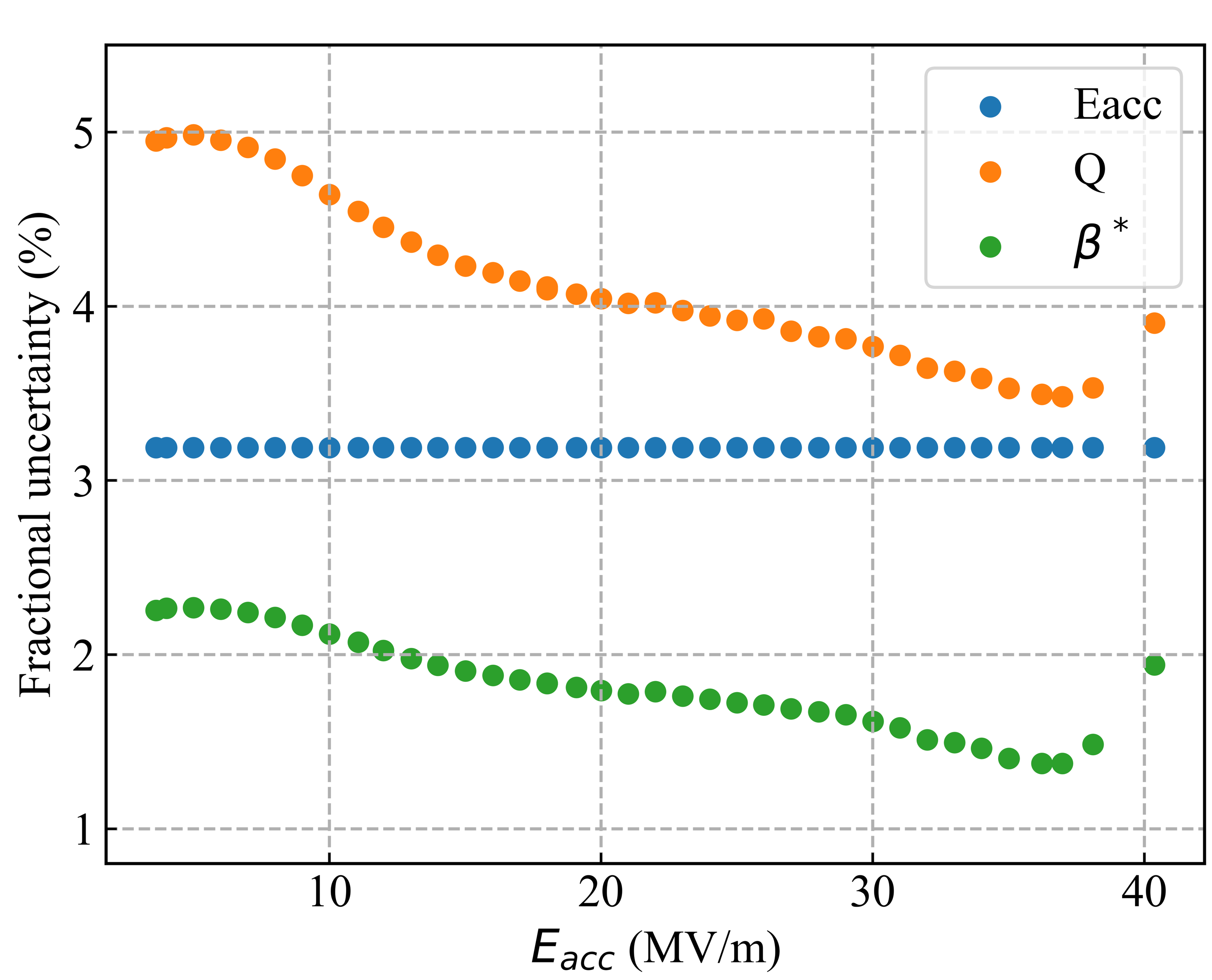

Fractional uncertainties on E_{acc}, Q_0 and β^* as a function of E_{acc}

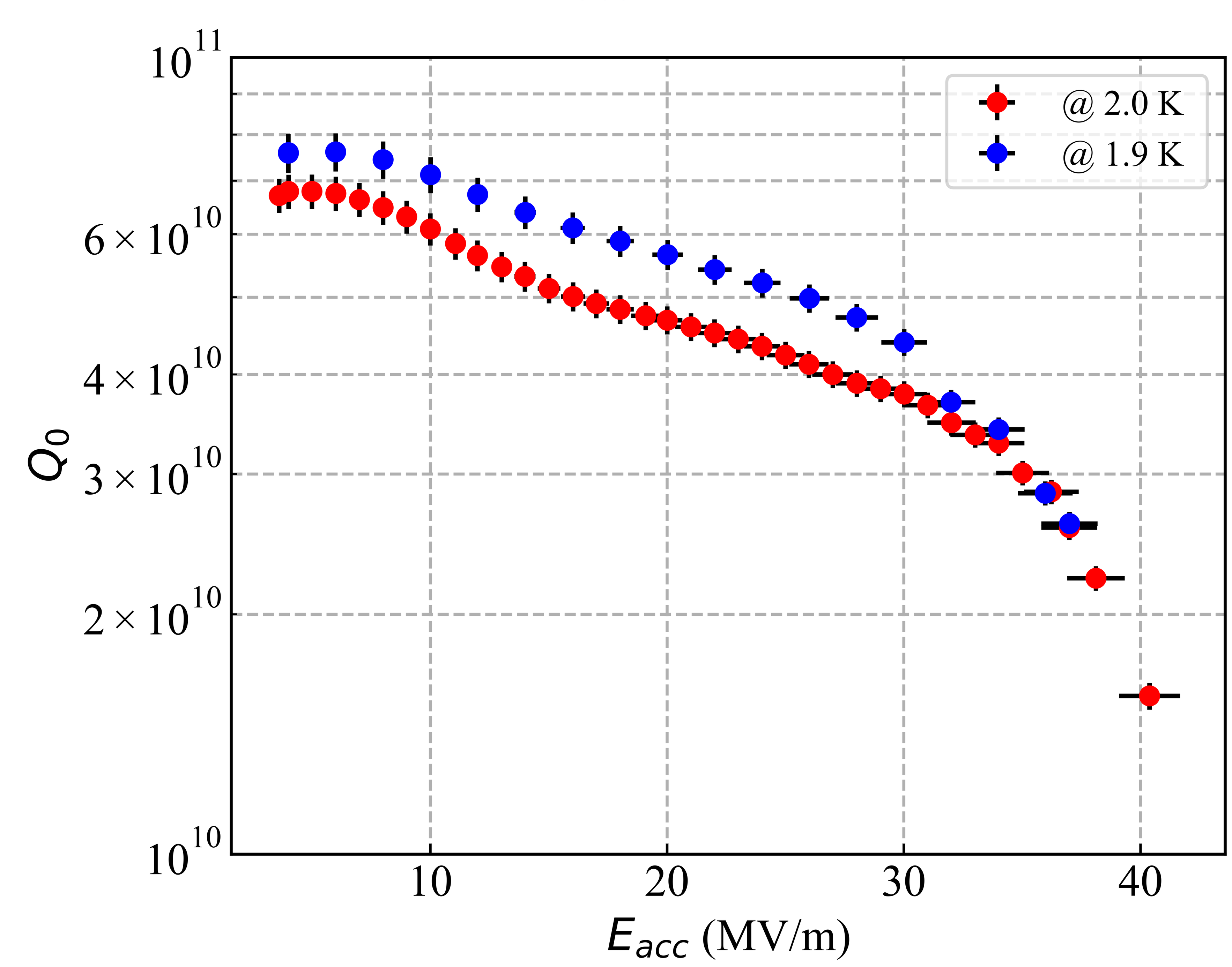

Vertical test results of 650 MHz single-cell cavity with Error bar

* Correspondence to: limeng@ihep.ac.cn

Preliminary design consideration for CEPC fast luminosity feedback system

Meng Li[1,2], Philip Bambade[3], Dou Wang[1], Haoyu Shi[1], Jianchun Wang[1], Jie Gao[1], Sha Bai[1] Shujun Wei[1], Xin Shi[1], Yunyun Fan[1], Yanfeng Sui[1,2], Ye He[1], Yiwei Wang[1], Yuan Zhang[1,2] Yuanyuan Wei[1], Yuhui Li[1], Zhijun Liang[1]
[1]Institute of High Engergy Physics, Chinese Academy of Sciences; [2]University of Chinese Academy of Sciences; [3]Laboratoire de Physique des 2 infinis Irène Joliot-Curie–IJCLab

Introduction

With very small beam sizes at IP (several tens of nanometers in the vertical direction) and the presence of strong FFS quadrupoles in the CEPC, the luminosity is very sensitive to the mechanical vibrations, requiring excellent control over the two colliding beams to ensure an optimum geometrical overlap between them and thereby maximize the luminosity. Fast luminosity measurements and an IP orbit feedback system are therefore essential. In this paper, we will show the preliminary design consideration for a fast luminosity feedback system at CEPC.

Orbit feedback methods

There are two methods for the IP orbit feedback system at CEPC[1,2,3]:

- **Beam-beam deflection driven method [vertical]**

The offset at the IP is too small to be accurately measured, but due to the beam-beam effect, which can introduce an deflect angle, and then transfer to a larger offset, by measuring this beam orbit with BPMs upstream and downstream of the IP , we can estimate the offset at the IP and the sign.

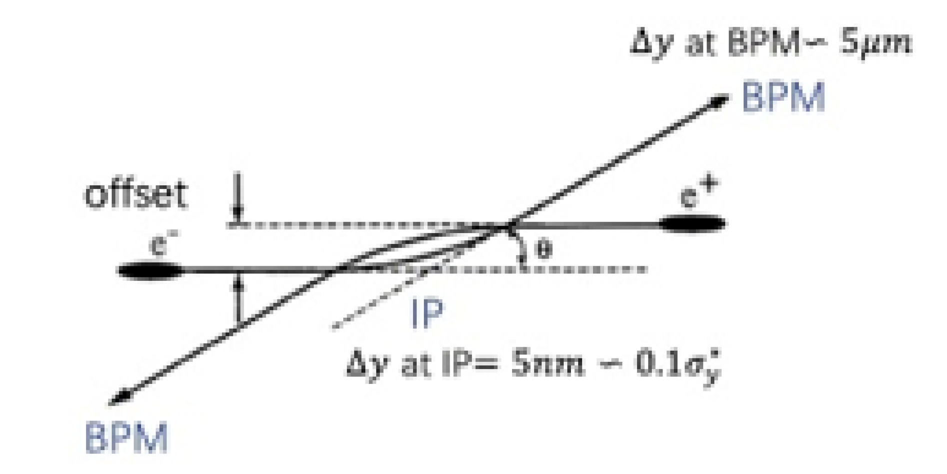

$$\Delta y'_{\pm} = -\frac{r_e N_{\mp}}{\gamma_{\pm}\sigma^*_{y\mp}(\tilde{\sigma}^*_{x\mp}+\sigma^*_{y\mp})}\Delta y_{IP} \qquad \Delta y_{BPM} = \sqrt{\beta^*\beta_{BPM}}\Delta y'$$

- **Luminosity driven system [horizontal]**

Based on the measurement of the luminosity, we can know the offset between two beams, but cannot easily know its sign. And many other effects may also cause luminosity changes at relatively low frequency, should introduce a dithering with certain frequency.

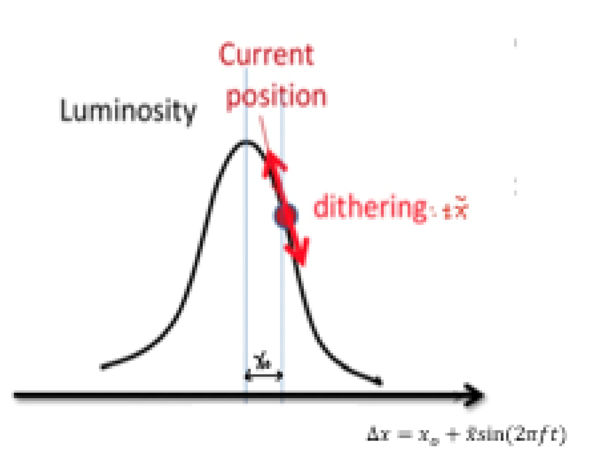

$$L(x) = L_0\left(1 - \frac{x_0\tilde{x}}{\Sigma_x^2}\sin(2\pi ft) - \frac{\tilde{x}^2}{2\Sigma_x^2}\sin^2(2\pi ft)\right)\exp\left(-\frac{x_0^2}{2\Sigma_x^2}\right)$$

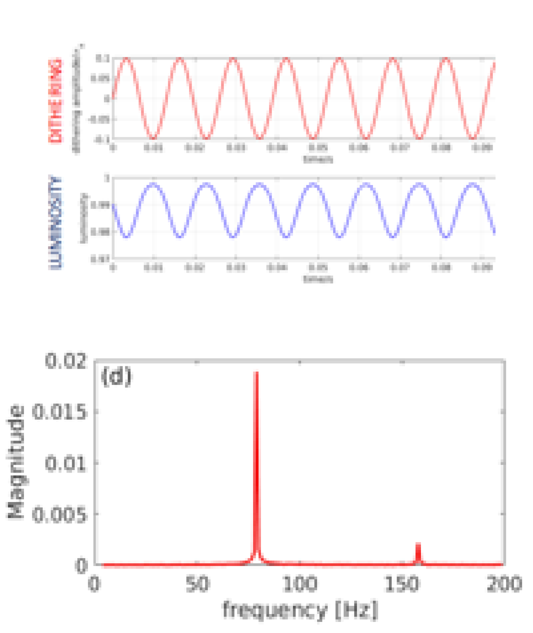

Vertical—Beam-beam deflection driven method

Our preliminary scheme is to place 4 sets of BPMs on both sides of the IP for each ring, which located near the maximum betay. In this way, the current resolution of BPMs is good enough for vertical IP orbit feedback.

CEPC	N_{bunch} $[10^{11}]$	β^*_x/β^*_y $[m/mm]$	σ^*_x/σ^*_y $[\mu m]$	ξ^*_x/ξ^*_y	$\Delta x_{IP}/\Delta y_{IP}$ 0.1σ $[\mu m/nm]$	$\Delta x'/\Delta y'$ $[\mu rad]$	$l_{IP\to BPM}$ $[m]$	BPM resolution
Higgs	1.3	0.3/1	14/0.036	0.015/0.11	1.4/3.6	-0.44/-2.49	0.85	0.3um@10Hz
Z	1.4	0.13/0.9	6/0.035	0.004/0.127	0.6/3.5	-0.12/-3.1		
W	1.35	0.21/1	13/0.042	0.012/0.113	1.3/4.2	-0.47/-2.98		
tt	2.0	1.04/2.7	39/0.113	0.071/0.1	3.9/11.3	-4.85/-2.63		

f[Hz]		GM	Correct	Measure	BPM resolution
HEPS	H	<1	10	100	**1um@100Hz**
	V	5	50	500	**2um@500Hz**
BEPC	H	0.02	0.2	2	0.1um@2Hz
	V	50	500	5000	**7um**@5kHz
KEK	H	0.1	1	10	0.3um@10Hz
	V	50	500	5000	7um@5kHz

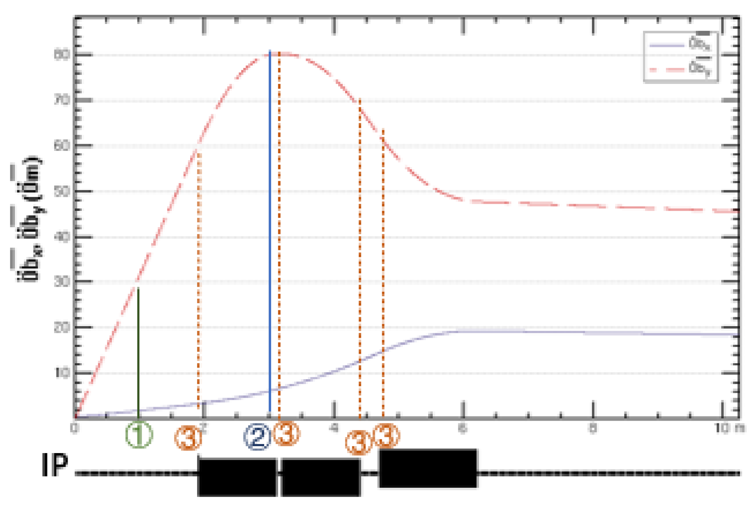

① The location of the current designed BPM → *not good enough for both direction*

$$\Delta y_{BPM} = \sqrt{\beta^*\beta_{BPM}}\Delta y' \approx s * \Delta y' = 2.2um \approx 1res@500Hz$$

$$\Delta x_{BPM} = \sqrt{\beta^*\beta_{BPM}}\Delta x' \approx s * \Delta x' = 0.4um \approx 0.4res@100Hz$$

② If place BPM at or near β_{ymax}-location → *get a larger offset at BPM*

$$\Delta y_{BPM} = \sqrt{\beta^*\beta_{BPM}}\Delta y' = -6.3\mu m \approx 3res@500Hz$$

③ If use multiple BPMs → *can reduce the requirement for BPM resolution*

$$\Delta y_{BPM}(n_{BPM}) \approx (\sqrt{n} * 3)\ res@500Hz$$

Horizontal—Fast Luminosity Monitor

The fast luminosity monitor based on radiative Bhabha at zero degree, which has a very large cross section ($\approx 150mbarn$). Find 3 possible detector positions where the loss rate is large enough and radiative Bhabha at zero degree process dominates over the sum of other particles loss processes.

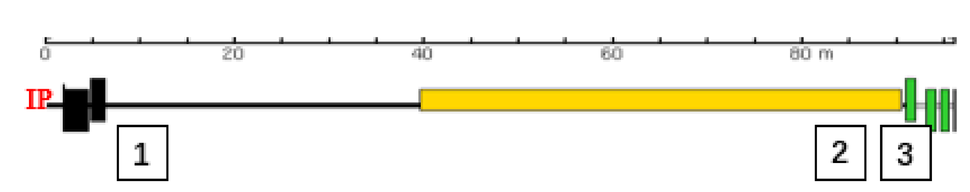

	Position1→ $10m$	Position2→ $84m$	Position3→ $90.5m$
Average Number detected/BX	~3.4(Two sides)	~3(One Side)	~3.2(One Side)
Average Bhabha Number /1ms	~2830	~2500	~2670
Expected measurement accuracy	1.9%@1kHz	2%@1kHz	1.95%@1kHz
Average Energy of Pris	~24 GeV	~70 GeV	~75.3 GeV
Average Hitting Angel	~1.7E-4 rad	~7E-4 rad	~7E-4 rad
T_{max} in mm	88.32	103.85	104.91
Detector Size assumed	5*20 cm²	3*15 cm²	3*15 cm²
Backgrounds	SR Photons in 1 Side	-	-
Pros	Measurement affected by beam-beam deflection angle, two detectors	signals only on one side, measurement quite independent of beam-beam deflection angle	
Detector technology	LGAD; SiC; Diamond		

Conclusion

- **Fast Luminosity Tuning System, including fast BPMs and fast luminosity monitor, would be necessary for CEPC.We already have some candidate positions and potential detector solutions.The detailed design of the detectors is get started.**
- **More detailed simulations needs to be done to study more, including determine the detailed location and quantity of BPMs and the design of detectors and feedback.**

[1] Y. Funakoshi et al., “Interaction point orbit feedback system at SuperKEKB”, in Proc. 6th Int. Particle Accelerator Conf. (IPAC’15), Richmond, VA, USA, May 2015.
[2] D. El Khechen, “Fast Luminosity Monitoring Using Diamond Sensors for SuperKEKB”, PhD thesis, Université Paris-Sud, Orsay, France, 2016.
[3] C. G. Pang et al., "A fast luminosity monitor based on diamond detectors for the SuperKEKB collider", Nucl.Instrum.Meth. A931 (2019) 225-235.

Progress in the design Of CEPC Detector Beampipe

Abstract

There are five components in CEPC dector beampipe,including the extending Al pipe,the central Be Pipe,air channel,carbon fiber cylinder and combination flange.In addition, three detectors are installed on Beampipe: BPM, Lumical and Vertex.The main update of this design includes the addition of a detector BPM,and the extending pipe changed from conical pipe to gradient runway.

Detailed Structure

The overall two-dimensional cross-section of the beampipe is shown in the following figure: the total length is 1400mm.

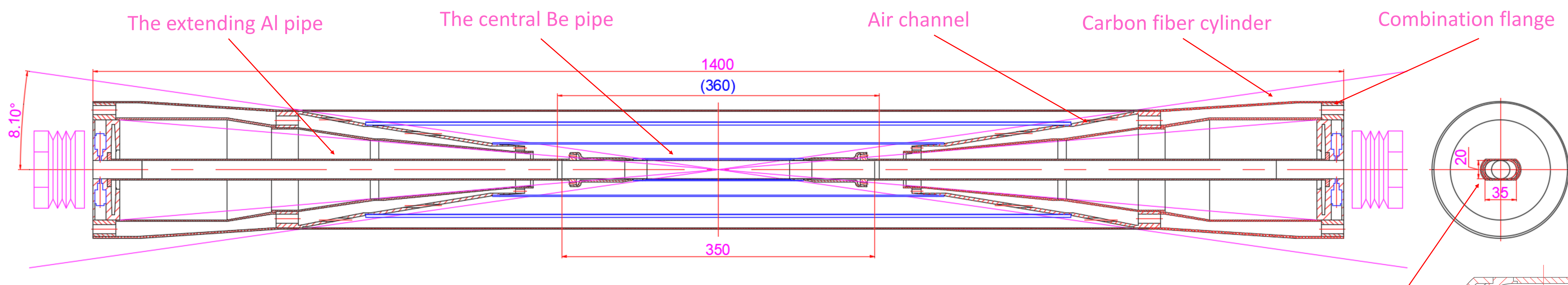

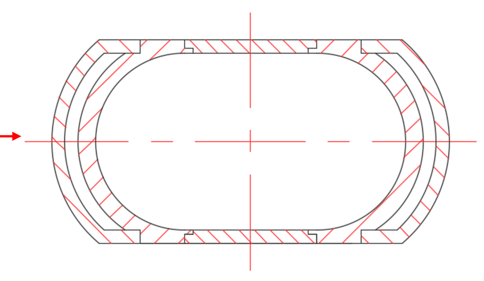

Extending pipe
Both sides : Double
Top and Bottom : Single

Structure of central Be pipe

The center of the beampipe adopts a double-layer Be pipe structure, with a length of 350mm. The wall thickness of the inner Be pipe is 0.2mm, and the wall thickness of the outer Be pipe is 0.15mm. There is a 0.35mm cooling medium gap between the double layer Be pipes, which is filled with cooling oil.

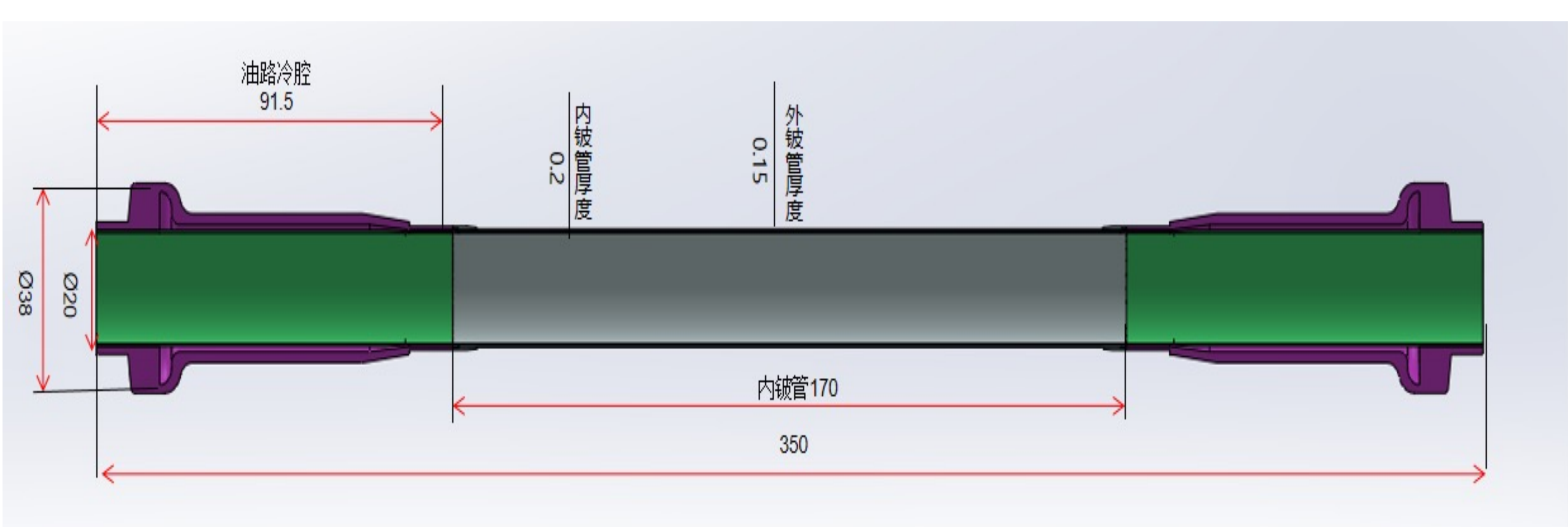

Structure of extending Al pipe

The total length of the extending Al pipe is 525mm, and its cross-section is a gradient runway structure. Two 1.5 or 2mm thick Be sheets is embedded on it, and the Lumical detector is placed on the Be sheets.

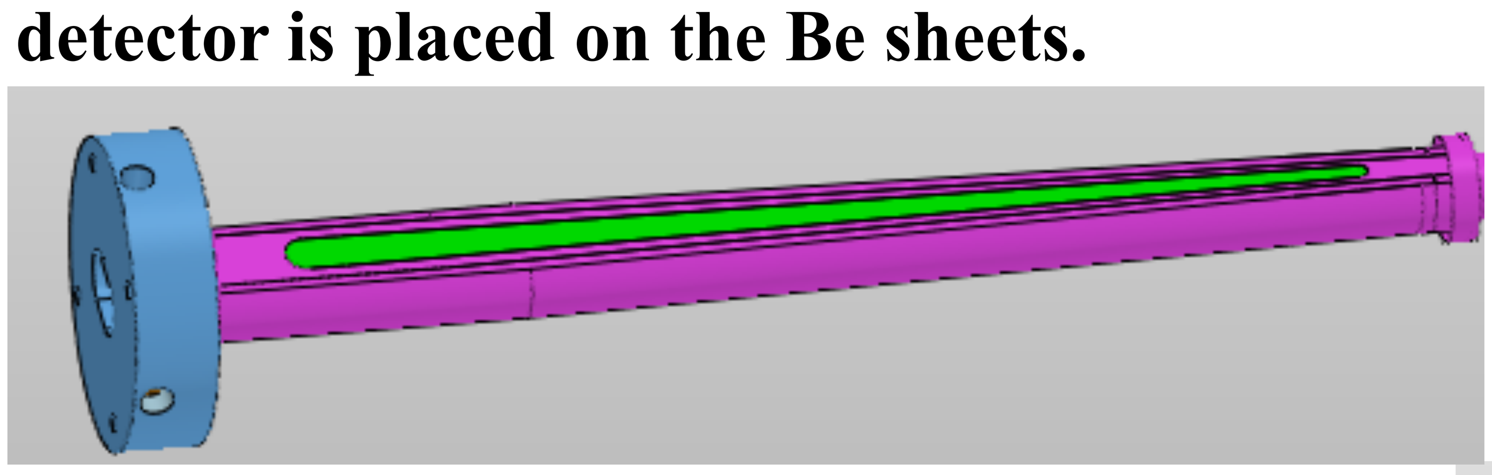

Be sheets(1.5 or 2mm)

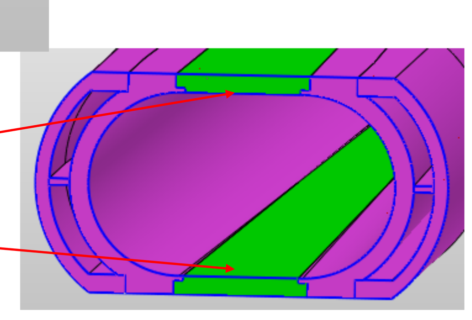

Thermal analysis --- Beampipe

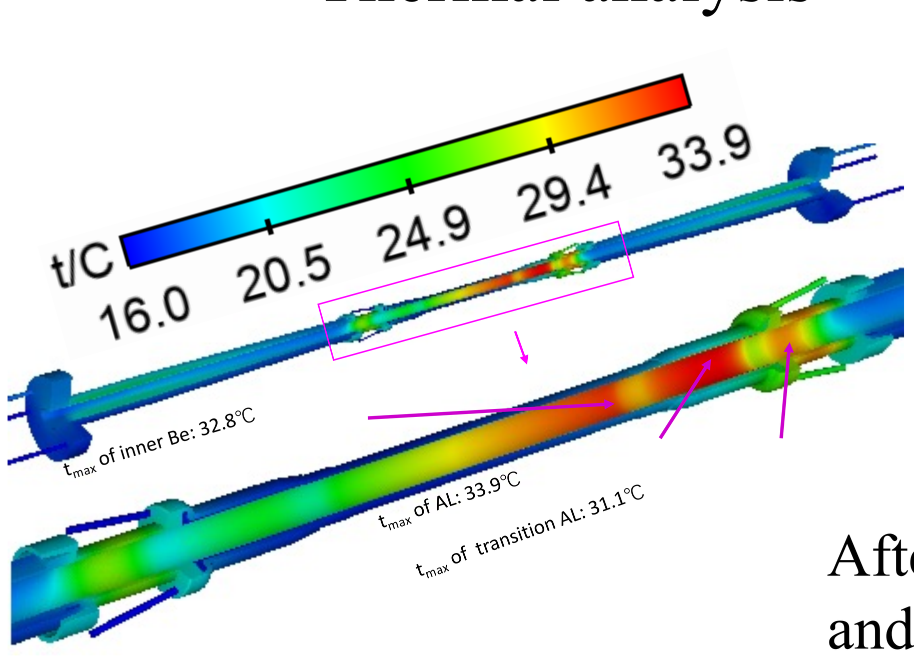

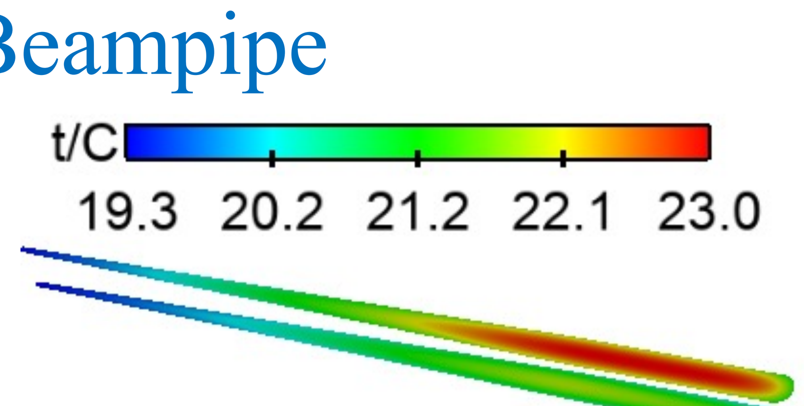

t_{max} of outer Be in expending pipe: 23℃

After simulation analysis, oil cooling and water cooling meet the temperature conditions.

The following are three-dimensional diagrams of the installation for three types of detectors: BPM, Lumical, and Vertex.

Installation --- BPM and Lumical

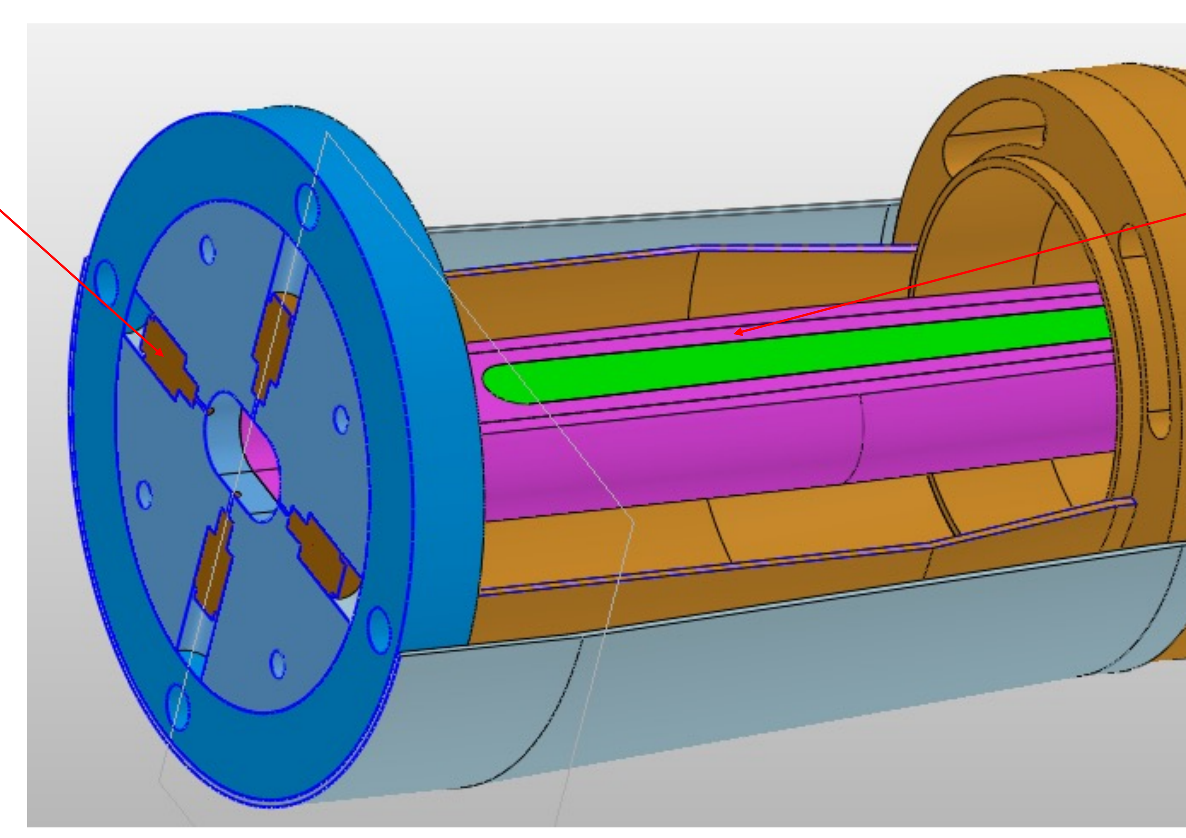

At present, the structure of Lumical has not been designed, but space has been reserved here for installing Lumical.

The Vertex detector contains only barrel part which consists of three double layers.

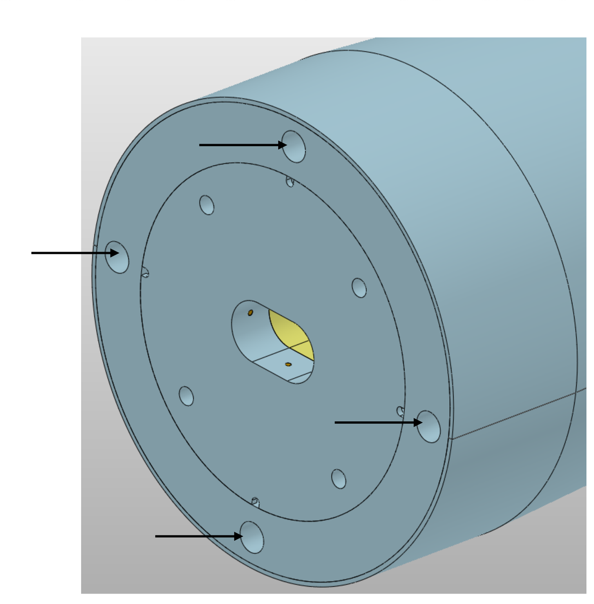

Four air inlets

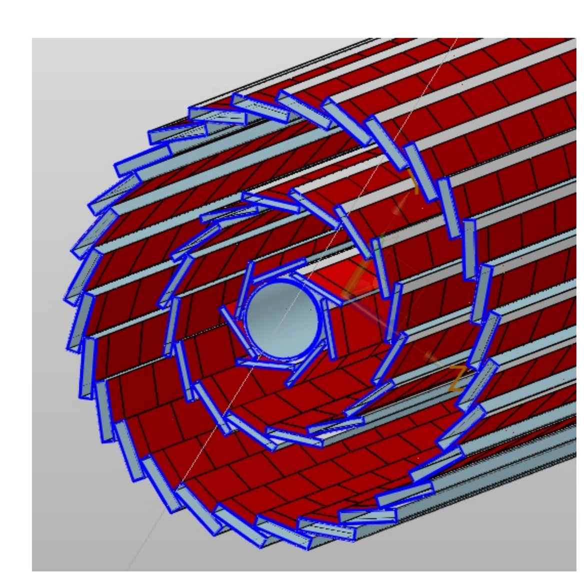

Three double layers

Cooled structure : Three layer air cooled channel

Design requirement
T ≤ 20 °C
△T < 10 °C or 7 °C
Vibration < 1μm

Question:

Can the Beampipe meet the requirements of air cooling and wind vibration?

CEPC Fast Luminosity Monitor with Silicon Carbide

Ye He[1,2] , Xin Shi[2]

Nanjing University[1]

Institute of High Energy Physics, CAS[2]

Introduction

To cope with the challenging beam condition at CEPC, we plan to build a fast luminosity monitor at CEPC with silicon carbide (SiC). By setting two detectors inside and outside the beam pipe, one can measure the Bhabha scattered particles and the secondary charged particles generated in the beam pipe. The luminosity is monitored by counting the number of Bhabha events with the goal of 2% accuracy at 1kHz rate.

Detecting method

Bhabha scattering is the major particle loss, and we can calculate the luminosity by counting the number of Bhabha particles.

Once we get the number of Bhabha scattering electrons (N), we can calculate the luminosity(L):

$$L = \frac{N}{\sigma \times T}$$

where σ is the cross section, T is frequency.

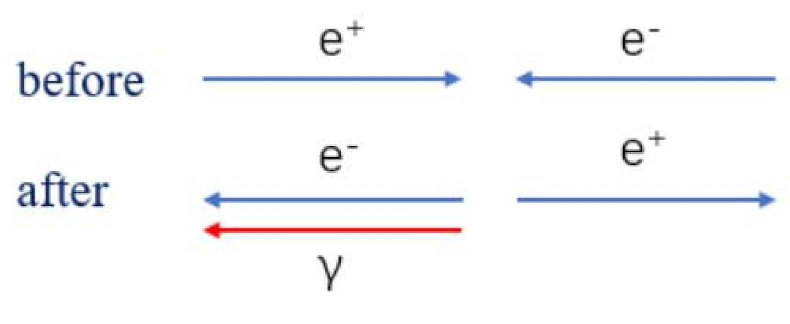

Bhabha scattering

Preliminary design of the detector

Our goal is to build a detector with 2% accuracy at 1kHz counting rate. Parameters of the electron is shown in the table behind. The detector can detect radiative Bhabha particles(e-) at zero degree and secondary particles after the electrons going through the 2mm copper pipe like the figure shows

energy	24 GeV
angle	1 mrad
interval	600 ns (Higss) 23 ns (Z)

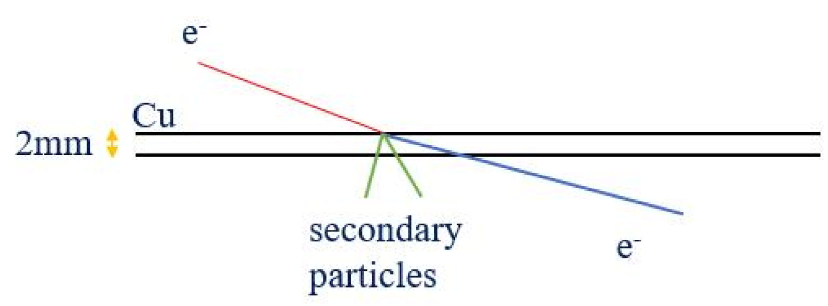

The detector is set at 10m downstream the IP. After preliminary simulation, 20cm×5cm is the best size.

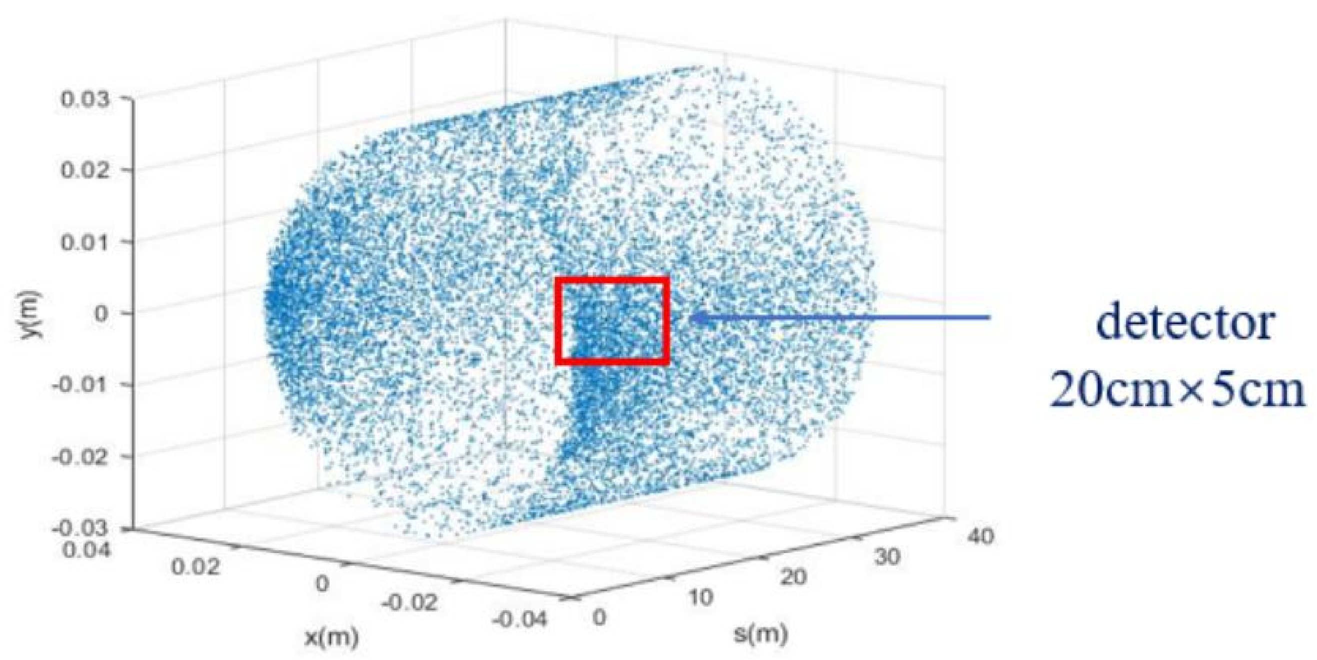

We choose to use silicon carbide sensors in the detector. We are going to design a readout board to carry the 20cm×5cm SiC sensor and get the signal generated by the sensor. The readout board can get the signal waveform when an electron hits the sensor. In this way, we can get all the waveforms in 1ms and send them to the back-end electronics to analyze.

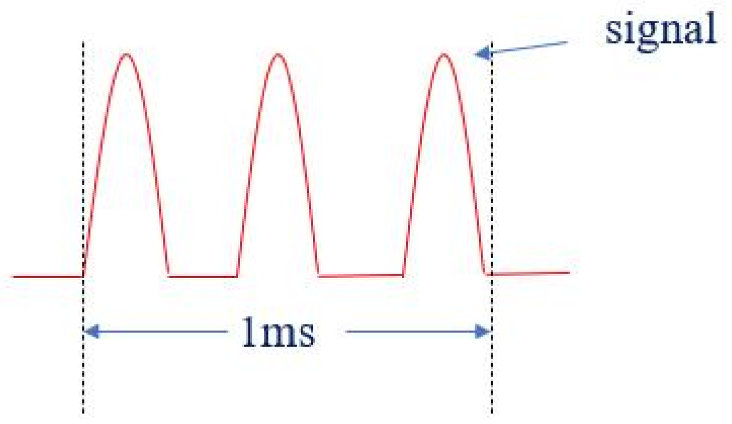

detector: generate signal by electrons

↓

readout board: get the waveform of the signal

↓

back-end electronics: calculate the number of electrons and luminosity

Readout system

We plan to use DRS4 chip to build readout system. The parameter of the chip is in the table below.

The DRS4 chip can change analog signal into digital signal which can be analyzed in the back-end electronics and send the digital signal to FPGA. Then we can calculate the luminosity.

Parameter of DRS4 chip

Bandwidth	950 MHz
channel	8
sampling rate	6 G/s
readout time	30ns

GEANT4 simulation

We use GEANT4 to simulate one 24 GeV hitting the 2mm copper pipe and use a 500μm silicon carbide sensor to detect it. The result and energy deposition are shown in the figures:

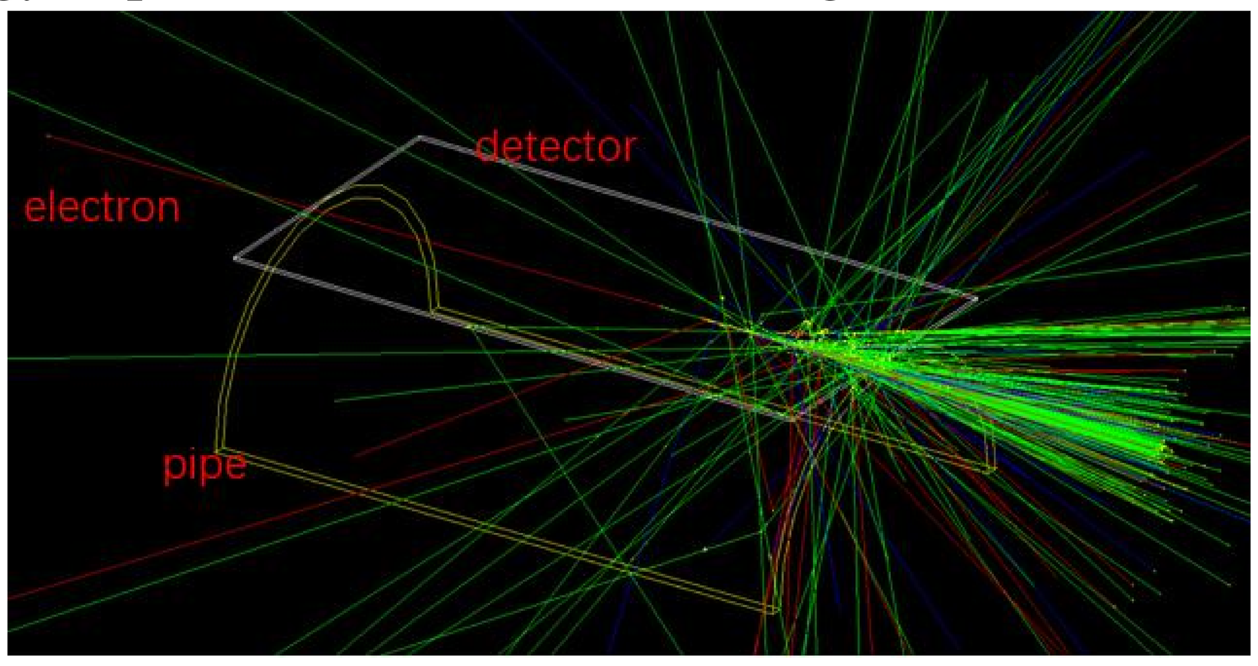

The mean value of energy deposition from single electron is 8 MeV, which means every 8 MeV energy in the SiC sensor represents an electron event. So we can calculate the total number of electrons by total energy deposition.

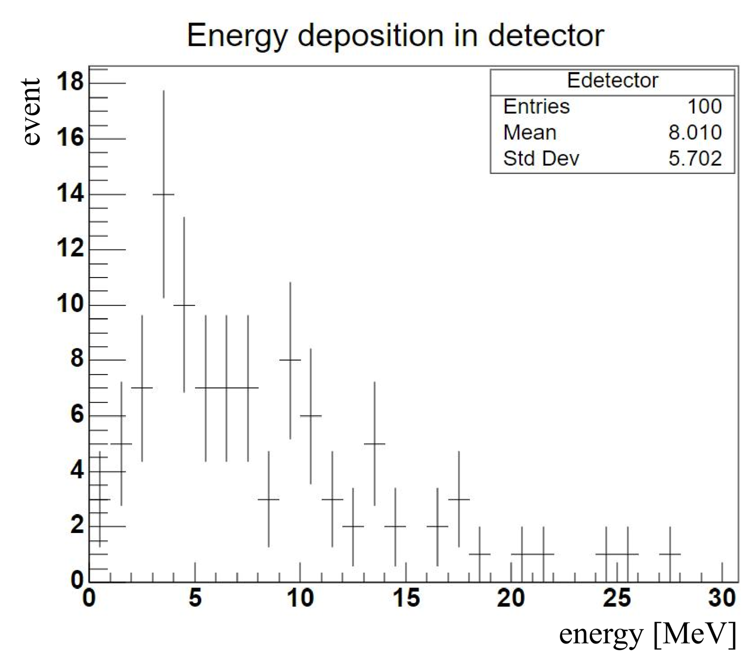

Summary and prospect

We introduce a fast luminosity monitor with silicon carbide which can be used in CEPC in this poster. We have finished preliminary design of the detector and have done GEANT4 simulation. Our goal is 2% accuracy at 1kHz counting rate and apply the fast luminosity monitor to CEPC successfully.

Institute of High Energy Physics
Chinese Academy of Sciences

环形正负电子对撞机
Circular Electron Positron Collider

CEPC workshop 2023
Nanjing, China
Oct 23 ~ Oct 27, 2023

Study of beam energy measurement using inverse Compton scattering approach

G. Y. Tang#, On behalf of CEPC Beam Energy Measurement Group

Institute of High Energy Physics, CAS, China

We discuss some schemes for measuring beam energy in a hundred-GeV collider using inverse Compton scattering approach. One is adjusting be in the collision angle or the incident photon frequency, the maximum energy of scattered photons could be in the range between 9 and 20 MeV. The systematic uncertainty of the beam energy could be in the range 2.1 to 8.1 MeV. The other is measuring the scattered lepton positions. Depending on whether the beam positions is measured directly, the systematic uncertainty could range from 1 MeV to 100MeV.

1. Introduction

- There are a lot of experiences in the world to measure beam energy from 1 GeV to 90 GeV, with accuracy 10^{-4}~10^{-5}. For the future lepton collider, beam energy measurement is a essential component.

Method	Accuracy	Facility	Energy range
$\gamma\mu\mu$	10^{-3}~10^{-4}	BESIII/Belle	3 ~ 11 GeV (CM energy)
Beam position monitor + magnet field measurement (BPM based)	10^{-4}	LEPII CLIC, ILC	45 ~ 500 GeV
Resonant depolarization (RDP)	10^{-5}~10^{-6}	LEP/LEPII, VEPP-4M, FCC-ee	1.5 ~ 90 GeV
Wire Imaging SR Detector (WISRD)	10^{-4}	SLC, ILC	45 ~ 500 GeV
Inverse Compton scattering (ICS)	10^{-5}	BEPCII, VEPP-4M, VEPP-2000	1.5~ 2 GeV

- Right figure illustrates a diagram of this system at the BEPCII . The green line, running from top-left side to top-right and the red line, running from top-right to top-left represent the beam directions passing through two bending magnets The CO_2 laser propagates along the red line in the middle of the diagram. Various optical devices are utilized to ensure an appropriate optical path. The scattered photons mainly travel in the horizontal direction . As the beam passes through the bending magnet and changes direction, the scattered photons maintain their original trajectory, allowing them to separate from the beam.

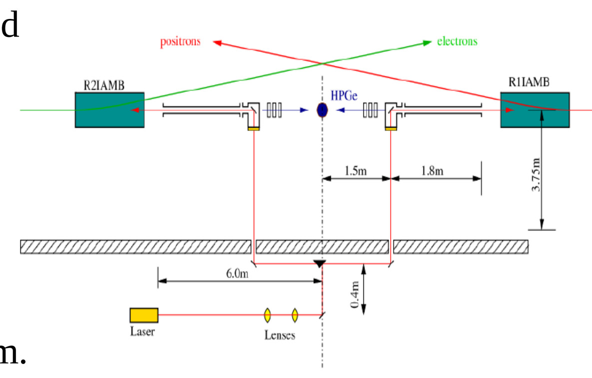

- The scattered photons are detected using a high purity Germanium (HPGe) detector is chosen for its superior energy resolution in the MeV energy region. The detected photon energy spectrum is depicted in the bottom figure. The beam energy is determined using three parameters: the angle α shown in the right figure below, the energy of the laser photon ω and the maximum energy of the scattered photons ω'. At the BEPCII, $\alpha = 0$, $\omega = 0.117$ eV, ω'~ 6 MeV. The accuracy of the beam energy is on the order of 10^{-5}.

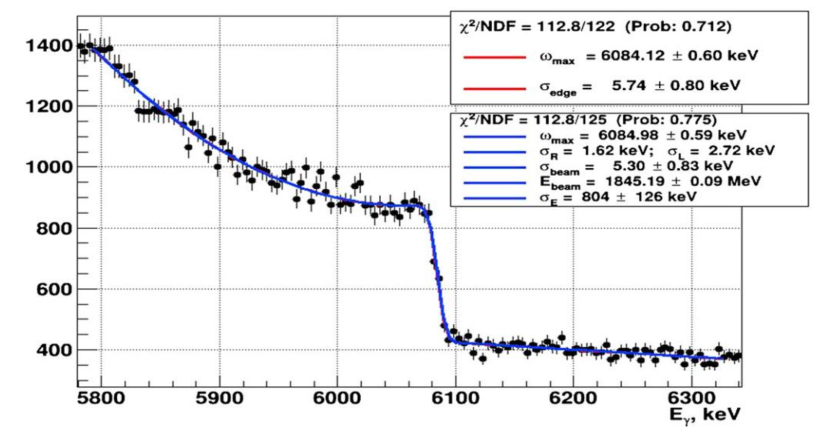

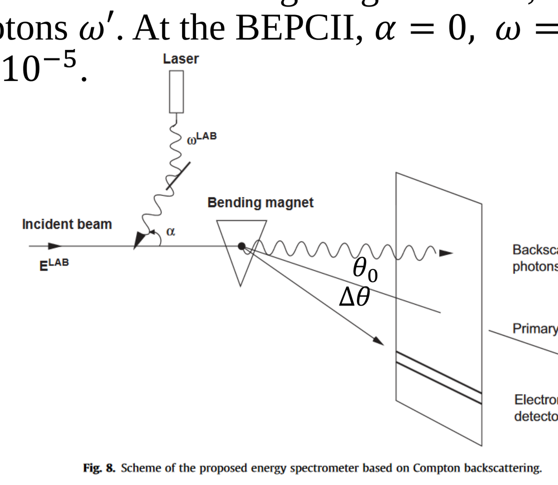

Nucl.Instr.Meth.A607 (2009) 340

- If we were to directly implement this system in a hundred GeV accelerator, the scattered photon energy would be in the range of several tens of GeV. However, accurately measuring such high energies and calculating the beam energy with a small uncertainty would be impossible. It is evident that there are three approaches to reduce the scattered photon energy:

method	Estimated accuracy
Adjusting the collision angle	2.1 ~ 8.1 MeV
Decreasing the laser photon energy	6 MeV
Measuring scattered lepton positions	1 MeV (beam position measured)
	108 MeV (without measuring beam position)

2. Adjusting the crossing angle

- The maximum energy of scattered photons as a function of angle α is shown in the figure below. The uncertainty of the beam energy propagates as follows:

$$\delta E_{beam} = \sqrt{\left(\frac{dE_{beam}(\alpha,\omega,\omega')}{d\alpha}\right)^2(\delta\alpha)^2+\left(\frac{dE_{beam}(\alpha,\omega,\omega')}{d\omega}\right)^2(\delta\omega)^2+\left(\frac{dE_{beam}(\alpha,\omega,\omega')}{d\omega'}\right)^2(\delta\omega')^2}$$

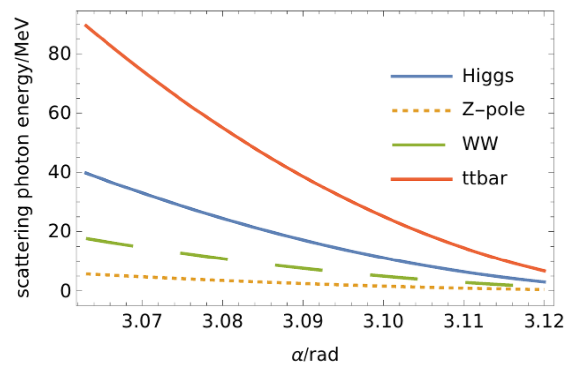

E_{beam}/GeV	α/rad	ω'/MeV	$\delta\alpha$/rad	$\delta\omega$/eV	$\delta\omega'$/keV
120	3.12	3.008	1.6×10^{-7}	1.95×10^{-6}	0.05
	3.102	10.629	3.0×10^{-7}		0.16
	3.093	15.230	4.1×10^{-7}		0.25
	3.086	19.932	4.6×10^{-7}		0.33

- We choose $\alpha < 20$ MeV, because of the range of HPGe detector. Assuming δE_{beam} = 1 MeV, and considering $\delta\omega = 0$ and $\delta\omega' = 0$, the uncertainties $\delta\alpha$ as a function of the angle α. Similarly, assuming $\delta\alpha = 0$, $\delta\omega' = 0$ and $\delta\alpha = 0$, $\delta\omega = 0$, we can obtain the uncertainties $\delta\omega$ and $\delta\omega'$ as functions of the angle α. These uncertainties are presented in Figures below. We have selected a series value for Higgs operation in Table above.

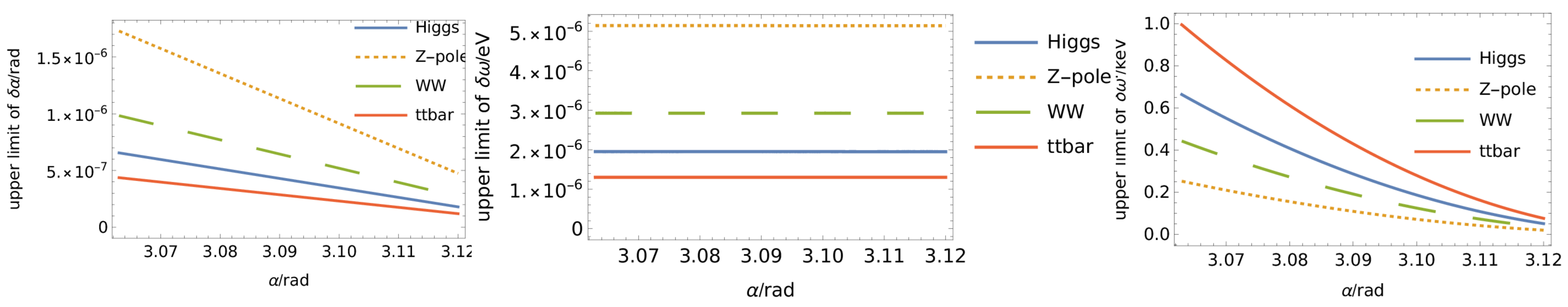

- The uncertainty of α would be control using a long beam orbit and a long laser path.
  - x_1, x_2, x_3 are the vertex
  - linear orbit 1km; BPM accuracy 100um; alignment uncertainty 50~100μm.

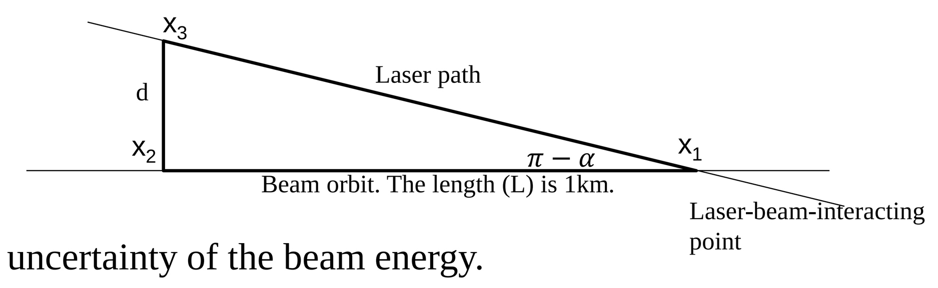

- $\delta\alpha \approx 1.42\times10^{-7}$rad.
  $< 4\times10^{-7}$rad.
  contribute a 0.5 MeV systematic uncertainty of the beam energy.
- Use beam and laser paras.: Laser Power: 50W; Photon energy: 0.117eV; Waist radius: 100um; Beam: 16.7mA, $\sigma_{x/y}$: 100/10um. Photon energy spectrum of SR and Compton scattering can be obtained in the figure below.
  - example: $\alpha = 3.093$
- HPGe Detector efficiency can be evaluated using Geant4.

	Dimension (mm)		Efficiency	
	Diameter	Length	9MeV	15MeV
Type I	57	62	1.4%	1.1%
Type II	80	82	4.5%	1.7%

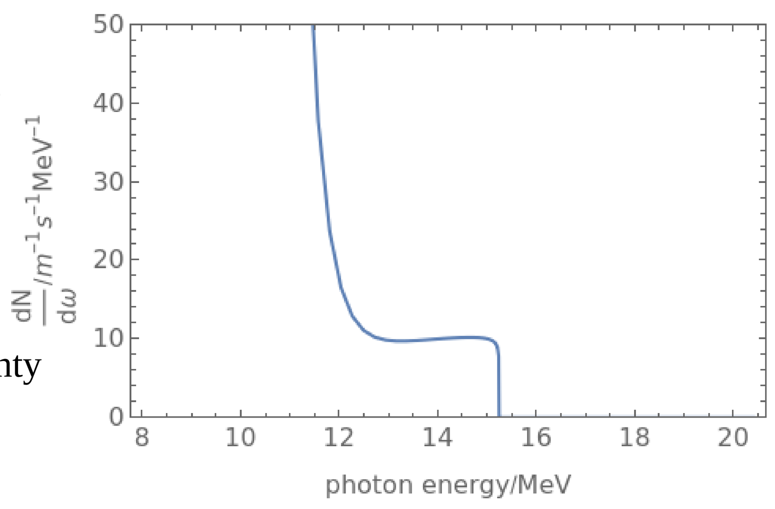

- Detect 200 events/hour. If assuming the same uncertainty of the Compton edge, it contributes a 2 ~ 8 MeV uncertainty of the beam energy
- Difficulty:
  - Higher power laser, smaller bunches, higher efficiency
  - Survived in Neutron-rich environment

3. Decreasing the photon energy (frequency)

- The maximum energy of scattered photons as a function of the wave length of the micro wave is shown in the figure below. We can select a series value for Higgs operation in Table below.

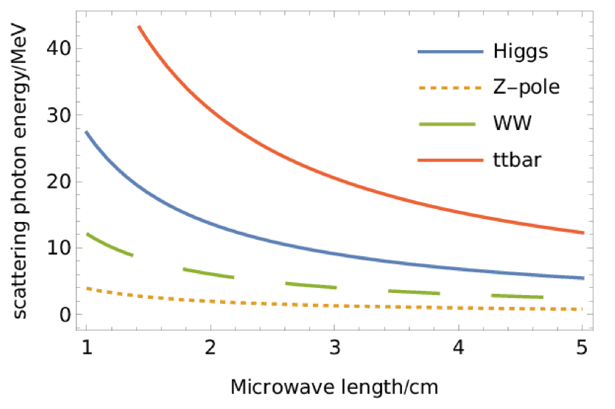

E_{beam}/GeV	Wave length/cm	ω'/MeV	$\delta\alpha$/rad	$\delta\omega$/eV	$\delta\omega'$/keV
120	9.10	3.005	0.008	2.27×10^{-10}	0.05
	3.04	8.996		6.79×10^{-10}	0.16
	2.30	15.192		1.15×10^{-9}	0.25
	1.37	19.969		1.51×10^{-9}	0.33

- These uncertainties are presented in Figures below. The uncertainty of the beam energy is estimated in Ref. Nucl. Instrum. Meth. A, 1026:166216, 2022.

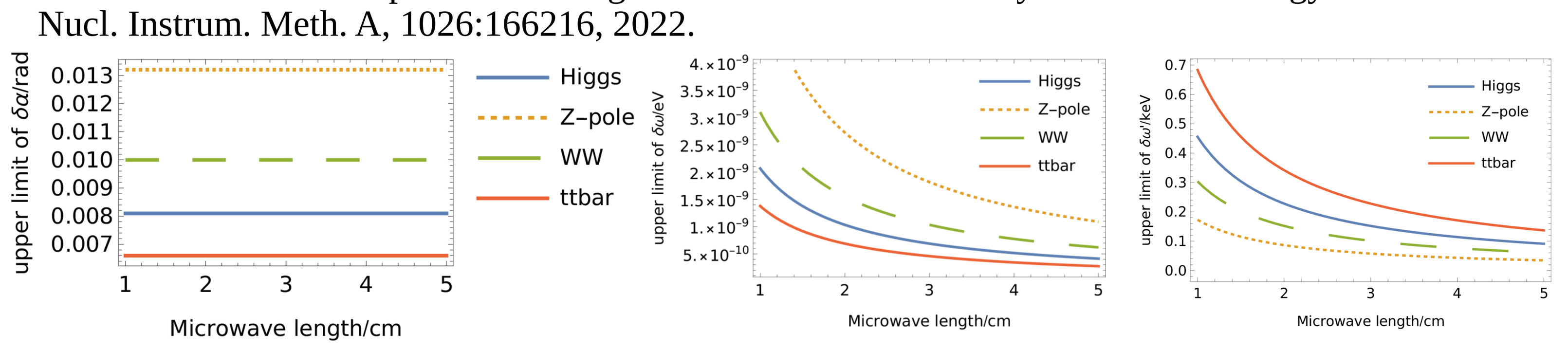

- The wave length is in the microwave band and we should find a suitable source. Notice that the existence of a Compton edge relies on the on-shell (plane-wave) photon and the energy-momentum conservation. The micro wave in a wave guide or cavity may not appropriate

4. Measuring scattered lepton positions

- Extract some bunches; Magnet field: 0.5T; the length of dipole: 3m; the drift distance between the bending magnet and detector: 500m. Three positions should be measured:
  - Backscattered photon position, X_γ (which is set as the axis origin).
  - Beam position, X_beam.
  - Position of the lepton with minimum energy after scattering, X_edge.
- If α=0, $E\_beam \sim \frac{(mc^2)^2}{4\omega}\frac{\Delta\theta}{\theta_0} \sim \frac{(mc^2)^2}{4\omega}\frac{X_{edge}-X_{beam}}{X_{beam}-X_\gamma} + O\left(\left(\frac{X_{edge}-X_{beam}}{X_{beam}-X_\gamma}\right)^2\right)+\cdots$
  - $O\left(\left(\frac{X_{edge}-X_{beam}}{X_{beam}-X_\gamma}\right)^2\right)$~$11.5MeV$;
- If requiring δE_{beam}<1MeV, the upper limits of positions measurement are listed above.

Beam energy	δX_{edge}	δX_{beam}	δX_γ
120GeV	$36\mu m$	$22\mu m$	$32\mu m$

- In Ref. RSI 91.3 (2020): 033109. A preliminary simulation shows the uncertainty of the beam energy is smaller than 1 MeV.

X_{edge}/m	$6.163503\pm2.6\times10^{-5}$
X_{beam}/m	$1.879339\pm6\times10^{-8}$
X_γ/m	0 (fixed)
E_{beam}/GeV	119.9993 ± 0.0010

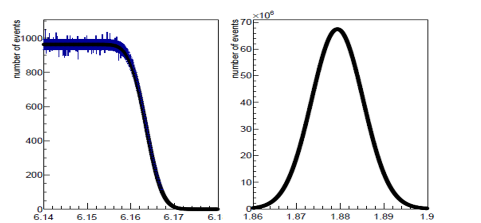

- Difficulty: How to measure bunch position?
  Diamond detector? BPM?

- To avoid the measurement of the bunch position, 2D fit is proposed in Ref. Nucl.Instr.Meth.A607 (2009) 340 and JINST 17 (2022) 10, P10014. Not only the beam energy but also the beam polarization can be measured.
  - Uncertainty of the beam energy @Z-pole ~ 10^{-4}

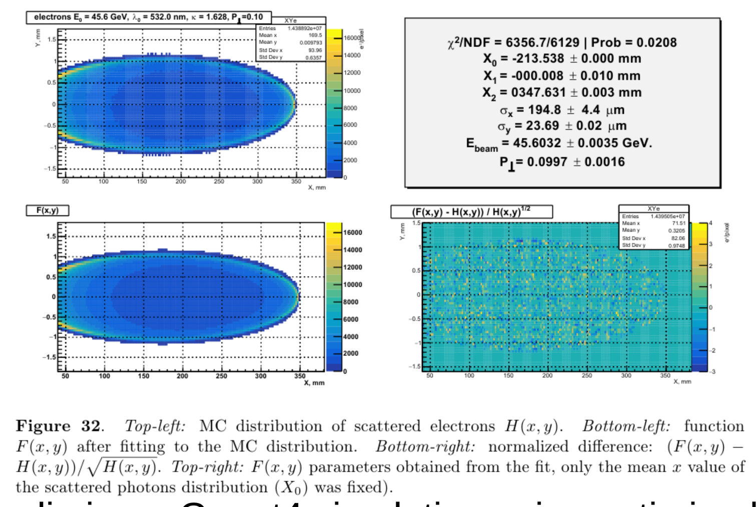

Figure 32: Top-left: MC distribution of scattered electrons $H(x,y)$. Bottom-left: function $F(x,y)$ after fitting to the MC distribution. Bottom-right: normalized difference: $(F(x,y)-H(x,y))/\sqrt{H(x,y)}$. Top-right: $F(x,y)$ parameters obtained from the fit, only the mean x value of the scattered photons distribution (X_0) was fixed).

- We optimize the parameters, then uncertainty of the beam energy @Higgs ~30 MeV (3×10^{-4})

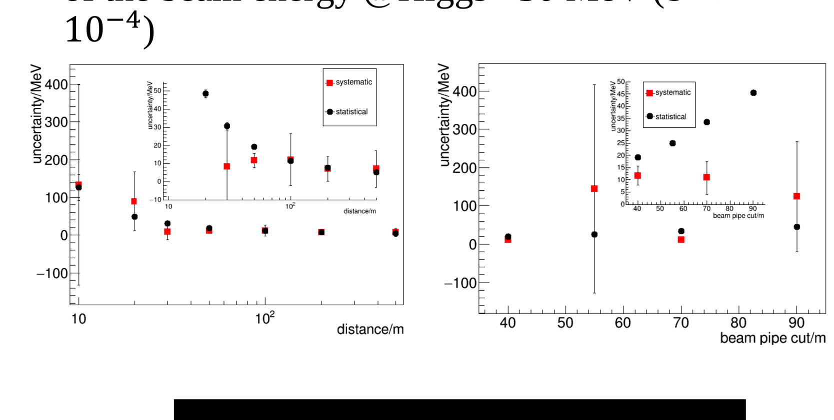

- A preliminary Geant4 simulation using optimized paras. is done.
  - Uncertainty ~ $\pm87(stat.) - 108(sys.)$ MeV.

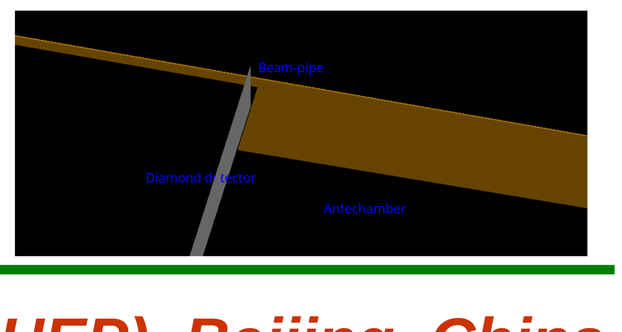

#tanggy@ihep.ac.cn